

2D Actuator Disk and Vertical Axis Rotor Model in the Wave-Current Unsteady Flow

Yuan Shan

Master of Science Thesis

2D Actuator Disk and Vertical Axis Rotor Model in the Wave-Current Unsteady Flow

MASTER OF SCIENCE THESIS

For the degree of Master of Science in Sustainable Energy Technology
(SET) at Delft University of Technology

Yuan Shan

October 22, 2013

Faculty of Applied Science (TNW) · Delft University of Technology



Copyright © Delft University Wind Energy Research Institute (DUWIND)
All rights reserved.

Abstract

A cross flow actuator based on a turbine concept is a possible choice for the harvest of the kinetic energy from a dynamic flow. Since there is a large potential of energy contained in the water movement of the ocean, it is fascinating to apply turbines to extract energy. In marine flows, currents can be described as steady since their flow velocities remain unchanged during long periods, while waves are treated as unsteady due to their variation within short periods. In some regions, the flow is a combination of both the current and the wave. Thus, it is interesting to understand how the turbine behaves during the operation in this unsteady flow.

The current work tries to model the marine turbines by numerical methods. Two branches are then studied separately. The first model is built within a 2D rotor scale in which the turbine is represented as an actuator disk. Case studies are built with different wave and current velocity scales. The second model studies the case of the Vertical Axis Turbine (VAT) by integrating the wave model with a 2D VAT panel code.

The simulation results from the actuator disk model suggest that it is more feasible to extract energy from the case when the current is dominant, while in the other cases, the flow is dominated by the unsteady response with large variations of power or even negative power output observed. The results from the VAT model show that for all the wave current combinations, the turbine can reach a regular periodic performance under the operation condition where the blade rotation period equals the wave period. The further study of the load behavior indicates that the turbine's response can be controlled by tuning the phase difference between the wave flow and the blade rotation.

Table of Contents

Acknowledgements	xi
1 Introduction	1
1-1 Fundamentals of marine wave current turbines	2
1-1-1 Energy capture and axial thrust	2
1-1-2 Operation and maintenance	3
1-2 Overview of the thesis	4
2 Actuator Disk Model and Blade Element Method	7
2-1 Actuator Disk Model	7
2-1-1 Disk Model without Wake Rotation	7
2-1-2 Disk Model with Wake Rotation	8
2-2 Blade Element Method	9
3 2D Model of Wave and Current Flow	13
3-1 Airy linear wave model	13
3-2 Scales of currents and waves	15
4 Unsteady Actuator Disk Model	19
4-1 Unsteady free-wake vortex method	19
4-2 Runge-Kutta Method	22
5 2D Potential Flow Panel Method (VAT)	25
5-1 Selecting the singularity element	25
5-2 Discretizing the geometry	26
5-3 Determining the influence coefficients and establishing the system of equations	26
5-4 Solving linear set of equations and secondary computing	27

6	Simulations for Different Wave Current Cases - 2D Actuator Disk	29
6-1	The current case - baseline actuator disk	29
6-2	Wave case	30
6-2-1	Wave case - constant force	30
6-2-2	Wave case - varying force	31
6-3	Current and wave	35
6-3-1	Current and wave - constant force	35
6-3-2	Current and wave - varying force	37
7	Simulations for Different Wave Current Cases - 2D VAT	41
7-1	The current case	41
7-2	Wave case	41
7-2-1	Arbitrary wave period	42
7-2-2	Wave period equal to rotation period	43
7-3	Wave and current case	48
7-3-1	Arbitrary wave period	48
7-3-2	Wave period equal to rotation period	50
8	Conclusions and Recommendations	53
8-1	Conclusions	53
8-2	Recommendations	54
	Bibliography	57
	Nomenclature	59

List of Figures

2-1	Actuator disc model of a wind turbine[1]	8
2-2	Annular streamtube and plane	9
2-3	Schematic of blade elements	11
2-4	Local element geometry and forces	11
3-1	Characteristic measures for an oscillatory wave[2]	13
3-2	Particle orbits according to the Airy theory[3]	14
3-3	X velocity amplitude (AmpV) VS elevation (Z)	16
4-1	Cross-section through an actuator surface[4]	20
4-2	Vortex shedding process	21
6-1	Wake Geometry of the current case at $TSTEP = 100$	30
6-2	Comparison of the induction factor from BEM and the free wake vortex model	31
6-3	Wake velocity oscillation within a wave period	32
6-4	Wake geometry of wave case, constant force, $t = 20T_w$	33
6-5	Wake geometry of wave case, constant force, $t = (20 + \frac{1}{4})T_w$	33
6-6	Wake geometry of wave case, constant force, $t = (20 + \frac{1}{2})T_w$	33
6-7	Wake geometry of wave case, constant force, $t = (20 + \frac{3}{4})T_w$	33
6-8	Wake geometry of the wave case with varying force	34
6-9	Power coefficient of the wave case with varying force	34
6-10	Induced velocity of the wave case with varying force	34
6-11	Wake geometry of the wave current case with constant force ($ALPHA = 1$)	35
6-12	Power coefficient of the wave current case with constant force($ALPHA = 1$)	36
6-13	Induction factor of the wave current case with constant force ($ALPHA = 1$)	37

6-14 Curve-fitting for the induction factor for wave current case with constant force ($ALPHA = 1$)	37
6-15 Wake geometry of wave current case with varying force ($ALPHA = 2, t = 3T_w$)	38
6-16 Wake geometry of wave current case with varying force ($ALPHA = 2, t = (3 + \frac{1}{4})T_w$)	38
6-17 Wake geometry of wave current case with varying force ($ALPHA = 2, t = (3 + \frac{1}{2})T_w$)	38
6-18 Wake geometry of wave current case with varying force ($ALPHA = 2, t = (3 + \frac{3}{4})T_w$)	38
6-19 Wake geometry of wave current case with varying force ($ALPHA = 2, t = 4T_w$)	38
6-20 Wake geometry of wave current case with varying force ($ALPHA = 2, TSTEP = 3000$)	38
6-21 Induction factor of the wave and current case with varying force, $ALPHA = 2$.	39
6-22 Wake geometry of the wave current case with varying force, $ALPHA = 0.5$. .	39
6-23 Induction factor of the wave current case with varying force, $ALPHA = 0.5$. .	40
7-1 Wake Geometry of the VAT (Current Case)	42
7-2 C_{Fx} over one rotation (Current Case)	42
7-3 Angle of attack over one rotation (Current Case)	42
7-4 Wake geometry after 1 rotation (Wave Case, $T_w = 5s$)	43
7-5 Wake geometry after 5 rotation (Wave Case, $T_w = 5s$)	43
7-6 Wake geometry after 10 rotation (Wave Case, $T_w = 5s$)	43
7-7 Wake geometry after 30 rotation (Wave Case, $T_w = 5s$)	43
7-8 X-component Force Coefficient (Wave Case, $T_w = 5s$)	44
7-9 Wake geometry of the wave case with $T_w = T_R$ (Start 0)	45
7-10 Wake geometry of the wave case with $T_w = T_R$ (Start $\frac{1}{2}\pi$)	45
7-11 Wake geometry of the wave case with $T_w = T_R$ (Start π)	45
7-12 Wake geometry of the wave case with $T_w = T_R$ (Start $\frac{3}{2}\pi$)	45
7-13 C_{Fx} of the wave case with $T_w = T_R$ (Start 0)	46
7-14 C_{Fx} of the wave case with $T_w = T_R$ (Start $\frac{1}{2}\pi$)	46
7-15 C_{Fx} of the wave case with $T_w = T_R$ (Start π)	46
7-16 C_{Fx} of the wave case with $T_w = T_R$ (Start $\frac{3}{2}\pi$)	46
7-17 C_{Fx} over one rotation of the wave case, $T_w = T_R$ (Start 0)	46
7-18 α over one rotation of the wave case, $T_w = T_R$ (Start 0)	46
7-19 Velocities relation of the wave case with $T_w = T_R$ (Start 0, $\theta = 45^\circ$)	47
7-20 Velocities relation of the wave case with $T_w = T_R$ (Start 0, $\theta = 135^\circ$)	47
7-21 Velocities relation of the wave case with $T_w = T_R$ (Start 0, $\theta = 225^\circ$)	47
7-22 Velocities relation of the wave case with $T_w = T_R$ (Start 0, $\theta = 315^\circ$)	47
7-23 Velocities relation of the wave case with $T_w = T_R$ ($\theta = 45^\circ$, Start 0)	49
7-24 Velocities relation of the wave case with $T_w = T_R$ ($\theta = 45^\circ$, Start $\frac{1}{2}\pi$)	49

7-25	Velocities relation of the wave case with $T_w = T_R$ ($\theta = 45^\circ$, Start π)	49
7-26	Velocities relation of the wave case with $T_w = T_R$ ($\theta = 45^\circ$, Start $\frac{3}{2}\pi$)	49
7-27	Wake Geometry of the wave current case with $T_w = 5s$ ($ALPHA = 0.2$)	50
7-28	C_{Fx} of the wave current case with $T_w = 5s$ ($ALPHA = 0.2$)	51
7-29	Wake Geometry of the wave current case with $T_w = T_R$ ($ALPHA = 0.2$, Start π)	51
7-30	C_{Fx} of the wave current case with $T_w = T_R$ ($ALPHA = 0.2$, Start π)	52

List of Tables

3-1	Classification of wave types[2]	14
3-2	Wave parameters	16
3-3	Wave period VS Amplitude of the wave velocity	17
3-4	Scales with different wave and tidal velocity combination from real sea states	17
3-5	Scales with different wave and tidal velocity combination for modeling	18
6-1	Induction factor features of different wave current cases with constant force	36
6-2	Induction factor features of different wave current cases with varying force	40

Acknowledgements

This is a journey. A journey with wonderful scenery all the way. Now, I am standing at the transfer station of my life. Thank you for being my companion and sharing all the lovely moments with me.

Firstly, I would like to thank Dr. Carlos Simão Ferreira for the supervision and instruction through the whole thesis project. What I learned from the stimulating and inspiring discussion is not only how to complete the thesis work, but also the academic thinking pattern and self-development. Furthermore, I want to acknowledge Prof. Gijs van Kuik for spending the afternoon together with us watching the "cute but puzzling" movies of the wake development and providing inspiring suggestions. I also would like to express my thanks to Dr. A. Palha da Silva Clerigo for your help with the model integration. I should tell you that it is so cool watching you typing codes which feels like watching "The Matrix".

Special thanks to Chen Qiuhua, Zhang Ye and He Chengguang to be my "daily supervisors" to stimulate me during every talk. Also, I want to thank Chidambaresan Krishnaswami, Lento Manickathan, Mark Schelbergen and Rob Mulders to be my office mates. The office is always a happy and lovely place with you guys.

Moreover, I would like to thank my friends: Daniel, Hugo, Paula, Nishant, Lin Jing, Jia Yifan, Cathi, Deleram, Suthi, Francesca, Vini, Wang Yiran, Chen Yue, Zheng Lu, Peng Yuhui, Yang Dan and Xu Yaolin; for all the moments that we are together. You are always supporting me and bringing joy to me.

Last but not least, to my family, my dear dad and mom, who are always there with me.

I love you all.

Delft, University of Technology
October 22, 2013

Yuan Shan

Master of Science Thesis

Yuan Shan

Chapter 1

Introduction

The ocean is a huge container which holds a tremendous amount of energy. It mainly produces energy in two types: thermal and mechanical. Waves, currents and tides are the branches of the mechanical type generated from the water movement in the ocean. To clarify the kinematic features of each movement, their definitions in oceanography will be briefly introduced.

Waves, or wind waves occur on the surfaces of the ocean. They are usually driven by the wind blowing and featured with oscillating motions. Wave models are introduced to describe the water particle's kinematics. Among the different wave theories and equations, the simplest model represents the waves with sinusoid shapes. This will be further depicted in Chapter 3. An ocean current is a continuous water flow in a dominant direction, for example, the Gulf stream which moves from the Gulf of Mexico northward through the Atlantic Ocean. The driving forces of an ocean current come from wind, Coriolis effect, temperature and salinity differences, tides and so on. Among them, tides are the main drives which are defined as the variation of the sea levels that are caused mainly by the gravitational attraction between the Earth and the Moon.

Tides and currents vary on the timescale of hours and therefore can be treated as steady flows within a certain short term. From this aspect, these two water movements will not be discussed separately in the later chapters and are together referred to as tidal currents. Meanwhile, waves oscillate within seconds and thus constitute the unsteady part of the flow. Then, the income flow in this thesis will be modeled as the superposition of tidal currents and waves.

The collection of tidal energy is usually achieved by turbines. One approach is to build a water reservoir. In this case, the flow is controllable but large civil works will be required and may affect the marine life and the local environment [5]. Alternatively, turbines can be directly located in the flow route and immediately turn the kinetic energy into electricity by the blade rotation. For the wave energy, the collection is always done by other conversion systems, typically, the oscillating water columns (OWC), point absorbers, attenuators and

the overtopping devices [6]. However, for the integration of tidal and wave energy, the turbine is chosen to be the energy convertor in this thesis. The above wave conversion systems will thus not be further introduced here.

As illustrated above, the energy conversion system here is mainly composed of the turbine and the generator. Waves and tidal currents will act together as the income flow. Under this circumstance, the turbine can be treated as the marine wave current turbine. The following sections will first review the fundamental issues involved in a marine wave current turbine system and then outline the main research questions of this thesis and the approaches to answer them.

1-1 Fundamentals of marine wave current turbines

The discussion on the fundamentals of the marine wave current turbines mainly takes the marine current turbine (MCT) system as reference. Since the energy carrier and operation environment is the same, the sea, these two systems are comparable. Several basic fundamental issues of MCT are discussed in Bahaj's paper [7]. The following parts will try to make a summary from Bahaj's while taking waves' influence into consideration.

1-1-1 Energy capture and axial thrust

The most fascinating factors of the tidal current energy are the predictable resources and the high energy density. The ocean current system is well studied by experts while the tide movements can be calculated from the patterns of the earth, sun and moon. Thereby, the harvest of the energy from tide can be planned in advance. The high energy availability can be easily explained by the high fluid density of the sea water. Generally, a tidal current turbine with the income flow speed at 2-3 m/s can produce four times as much energy as that of the rated power wind turbine per rotor swept area in one year [7]. With the assumption that in a certain time period, the velocity of the tidal current remains constant, V_c , the power contained in the flow is thus calculated as:

$$P_c = \frac{1}{2}\rho AV_c^3 \quad (1-1)$$

where ρ is the fluid density, A is the cross sectional area of the turbine.

However, the wave energy cannot be obtained by this equation since both the direction and the magnitude of the water particle velocity are varying with time. Furthermore, unlike the tidal currents, the wave behaviors have some randomness, which can however be predicted a few days ahead [8]. To predict the wave movements, wind wave models need to be involved. Since the analysis here will only take the typical statistics of the sea state around the UK, the details of the prediction models will not be further included.

To describe the wave behavior, several measures are defined in the metocean field. The instantaneous wave height, H , is the distance from crest to trough. From the observed record, one can get an average height measure in a given record length, typically about 20 minutes [2]. Wave period, T_w , is the time required for two successive wave crests/troughs to pass a fixed point. While these are the classical wave characteristics, the significant wave height and period, H_s and T_s are the most commonly used measures, which are defined as the average values of the highest 1/3 of the reported wave heights and periods [9]. With those metocean data, the power contained in the wave can be expressed by Eq. 1-2 [10]:

$$P_w = \frac{W\rho g^2 T_w H_s^2}{64\pi} \quad (1-2)$$

where g is the gravitational acceleration and W is the width of the wave front. One thing to note is that the power calculated in Eq. 1-1 only considers the kinetic energy of the current while Eq. 1-2 is obtained by estimating the rate of the potential energy change when the water falls from the crest into the trough in front of the wave.

As the high sea water density results in the high energy density, it also causes large thrust on the turbine. Assuming that the maximum resultant flow velocity is U_{max} and the turbine is designed with an axial thrust coefficient C_T , the maximum axial thrust, T_{max} is then:

$$T_{max} = \frac{1}{2} C_T \rho A U_{max}^2 \quad (1-3)$$

To resist the high loadings, robust structure is required, which will lead to an expensive construction. Furthermore, the oscillating wave movement will cause the variation of thrust in both the amplitude and the direction; and thus yields the fatigue problem. Therefore, the optimization to obtain a safe yet economic system is a key challenge in the marine turbine application.

1-1-2 Operation and maintenance

The most important factor that influences marine turbines' operation and maintenance is the sea water environment. The main obstacles are the corrosion, marine growth and the difficulties in accessibility, which are similar as those in the offshore and shipping industries [11]. Expertise and knowledge can be transferred from these industries to marine turbines and the prevention of the possible damages should be taken into consideration from the design phase through the whole life time of the turbines.

To solve the corrosion problem, anti-corrosive materials are used to manufacture or coat the structures. However, a more widespread and cost-effective way is to use the steel material with redundancy to offset the possible corrosion losses [7]. The marine growth is another common problem involved in the ocean-related engineering. For marine turbines, the organic fouling may drag or block the blades and thus result in low performance. Sometimes, the blade rotation can break the organism growth. Regular maintenance or telemetry is required

to inspect the marine growth and any other possible damages caused by debris in the sea water.

Considerate design can also increase the convenience of maintenance. Some units of the turbine can be well designed with raising facility to avoid the underwater inspection and repair work. Furthermore, the structure design can be optimized by placing components above the sea surface, for example, the generator of the vertical axis marine turbine. In addition, the maintenance should be carried out under a calm sea condition.

For the wave flow, as explained in the previous section, fatigue problem is involved. Therefore, design and experiments based on fatigue analysis need to be taken into account to avoid the possible fatigue damages.

Another factor that may influence the operation is cavitation. It is a phenomenon that vapor cavities are formed due to a relative low pressure. The formation of cavities may occur on the blade surface of the turbine where a rapid pressure jump exists. When the bubbles collapse, shock waves will be emitted, which may causes noise, vibration and damage to the blades.

Generally, the solutions to most of the sea generated problems can be found in offshore and shipping industries. The main limitation of the marine turbine development is the cost [11]. How to achieve the goals of operation and maintenance through economic way remains the key challenge for the application of marine turbines.

1-2 Overview of the thesis

The above fundamental issues of the wave current turbine are mainly based on the MCT; and the possible influence due to the unsteady wave flows is just empirically derived. For the MCT with horizontal axis, the turbine performance can be predicted by BEM modeling [12]. The scale model tests conducted by Bahaj and other researchers show the results that agreed well with BEM [13]. In the general BEM theory, the income flow is assumed to be steady. However, as illustrated above, waves will carry the oscillating movements to the flow. It is yet not clear whether the BEM model is valid under this circumstance. Therefore, we will try to study the turbine performance from the perspective of the wake. The main research questions of this thesis are:

1. How does the wake develop in the wave current flow?
2. What is the turbine's response to this kind of unsteady flow?
3. Is BEM still valid in the prediction of the unsteady turbine performance here?

The thesis will then try to answer the questions by the numerical modeling on a 2D rotor scale. The project is further divided into two parts. The first part represents the rotor with

an actuator disk and applies the unsteady free wake model to learn the wake development. Case studies are built for the situations where the ratios between the wave and current velocities are different. The second part is the study of the wave current turbine with vertical axis (VAT). This is done by the integration of wave model with the 2D VAT panel code developed by C.Simão. Ferreira [14]. Different wave current velocity combinations are also studied separately for the VAT model.

With the above research approach, the thesis is organized with 8 chapters. The first chapter briefly introduces the overall fundamentals of the marine current wave turbine to gain a primary understanding. Then the research questions are proposed which are the main drivers of this project. Chapter 2 explains the classical BEM theory which serves as the baseline for the result comparison in the latter chapters. Afterward, the linear wave model and the scales of currents and waves are illustrated in Chapter 3. The cases with various wave current combinations are then set up based on the real sea state. Furthermore, Chapter 4 studies the unsteady actuator disk model with a brief introduction of the optimization numerical method, the fourth-order Runge-Kutta method (RK4). Then, the basic computation steps of the panel method for the VAT model are outlined in Chapter 5. With all the inputs and model methods demonstrated in the previous chapters, Chapter 6 and 7 present and discuss the results from the unsteady actuator disk model and the VAT rotor model separately. Finally, Chapter 8 concludes the thesis work with remarks and recommendations for the future study.

Actuator Disk Model and Blade Element Method

This chapter reviews the blade element momentum (BEM) theory which is basically composed by two theories: actuator disk model (also well known as momentum theory) and blade element theory. The following sections will introduce them separately.

2-1 Actuator Disk Model

The actuator disk theory is first proposed by Rankine and Froude in the late 19th. The basic idea of the theory is to represent the real turbine rotor with an equal area disk. Several assumptions are involved [1]:

1. The disk is infinitely thin which means it is permeable for the air to pass through.
2. The fluid flow is considered to be incompressible, homogenous and steady.
3. No viscous effects are taken into account
4. Thrust and velocity are uniformly distributed on the disk.
5. Only the axial momentum balance is considered (1D).
6. Far up- and downstream pressure is the ambient pressure.

2-1-1 Disk Model without Wake Rotation

A typical rotor disk of a wind turbine is displayed in Fig. 2-1. The thrust (T) and the kinetic power extracted (P) are derived from the mass conservation law and the momentum balance. Without the consideration of disk rotation, it gives:

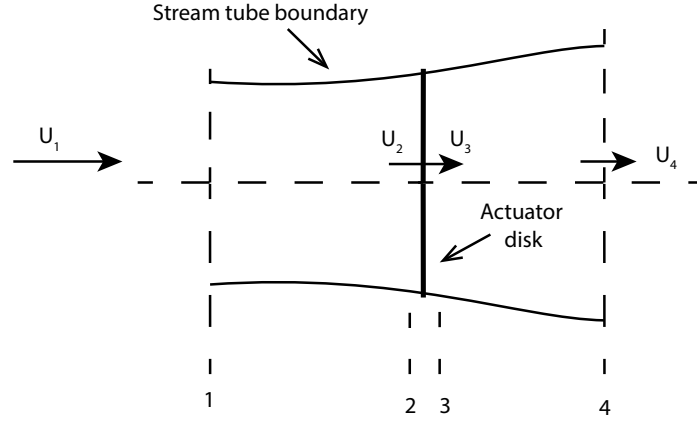


Figure 2-1: Actuator disk model of a wind turbine[1]

$$T = \dot{m}(U_1 - U_4), \quad P = \frac{1}{2}\dot{m}(U_1^2 - U_4^2) \quad (2-1)$$

where \dot{m} is the mass flow rate. With A is the disk area, ρ is the fluid density, $\dot{m} = (\rho AU)_1 = (\rho AU)_4$. With the axial induction factor, a , defined as:

$$a = \frac{U_1 - U_2}{U_1} \quad (2-2)$$

replace the income flow velocity U_1 with U and substitute Eq. 2-2 into Eq. 2-1, then:

$$T = \frac{1}{2}\rho AU^2[4a(1-a)], \quad P = \frac{1}{2}\rho AU^3 4a(1-a)^2 \quad (2-3)$$

The rotor performance is usually characterized with the non-dimensional coefficients:

Thrust coefficient:

$$C_T = \frac{T}{\frac{1}{2}\rho U^2 A} = 4a(1-a) \quad (2-4)$$

Power coefficient:

$$C_P = \frac{P}{\frac{1}{2}\rho U^3 A} = 4a(1-a)^2 \quad (2-5)$$

The maximum C_P is found when $a = \frac{1}{3}$. It is called the Betz limit, $C_{Pmax} = \frac{16}{27}$ and the corresponding thrust coefficient is: $C_T = \frac{8}{9}$.

2-1-2 Disk Model with Wake Rotation

When the rotor is rotating, it generates an angular momentum and causes the flow behind the rotor rotates in the opposite direction. Assume that the angular velocity of the rotor is Ω while the one of the wake is ω_{wake} . The angular induction factor, a' , is defined as:

$$a' = \omega_{wake}/2\Omega \quad (2-6)$$

Divide the rotor into radially independent annular elements (see Fig. 2-2). Now, for each annulus, the thrust is expressed as:

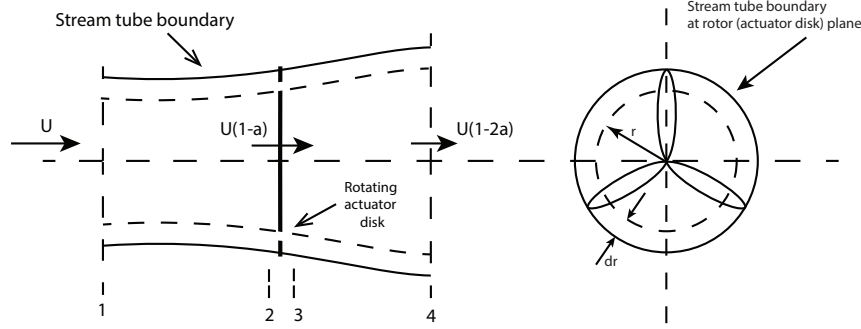


Figure 2-2: Annular streamtube and plane

$$dT = 4a(1-a)\frac{1}{2}\rho U^2 2\pi r dr \quad (2-7)$$

and the torque exerted on the annular element:

$$dQ = 4a'(1-a)\frac{1}{2}\rho U \Omega r^2 2\pi r dr \quad (2-8)$$

Since the model in this thesis does not involve the wake rotation case, detailed derivation will not be further explained here.

2-2 Blade Element Method

In the blade element theory, the blade is assumed to be divided into N segments as shown in Fig. 2-3. Two key assumptions are made:

- i) There are no aerodynamic interactions between different blade elements.
- ii) The forces on the blade elements are determined solely by the lift and drag coefficients.

For each blade element, the relative flow is composed of the wind velocity at the rotor, $U(1-a)$, and the velocity due to the blade rotation. When the blade is rotating with the speed Ω and the induced angular velocity at the blades from the wake rotation is $\omega_{wake}/2$, the rotational component velocity is thus:

$$\Omega r + (\omega_{wake}/2)r = \Omega r(1 + a') \quad (2-9)$$

An overview of the relationships of the flow velocities, angles and forces is shown in Fig. 2-4. Here, ϕ is the angle of relative flow velocity which is the sum of β , the local pitch angle (the

angle between the chord line and the plane of rotation), and α , the angle of attack (the angle between the chord line and the relative wind). The incremental lift force is represented as dF_L while dF_D is the drag force. dF_N is the incremental force normal to the rotation plane and dF_T is the tangential component.

The mathematical relationships between these parameters are:

$$\phi = \beta + \alpha \quad (2-10)$$

$$\tan\phi = \frac{U(1-a)}{\Omega r(1+a')} \quad (2-11)$$

$$U_{rel} = \frac{U(1-a)}{\sin\phi} \quad (2-12)$$

$$dF_L = C_l \frac{1}{2} \rho U_{rel}^2 c dr \quad (2-13)$$

$$dF_D = C_d \frac{1}{2} \rho U_{rel}^2 c dr \quad (2-14)$$

$$dF_N = dF_L \cos\phi + dF_D \sin\phi \quad (2-15)$$

$$dF_T = dF_L \sin\phi - dF_D \cos\phi \quad (2-16)$$

with C_l and C_d are the lift and drag coefficients which are determined by the airfoil shape. For the rotor which has B blades, the thrust (total normal force) on each segment is therefore:

$$dT = B dF_N = B \frac{1}{2} \rho U_{rel}^2 (C_l \cos\phi + C_d \sin\phi) c dr \quad (2-17)$$

and the torque can be computed from the tangential force:

$$dQ = B r dF_T = B \frac{1}{2} \rho U_{rel}^2 (C_l \sin\phi - C_d \cos\phi) c r dr \quad (2-18)$$

Recall the equations 2-7 and 2-8 from the momentum part, the calculation of thrust and torque links these two parts and thus forms the Blade Element Momentum (BEM) theory.

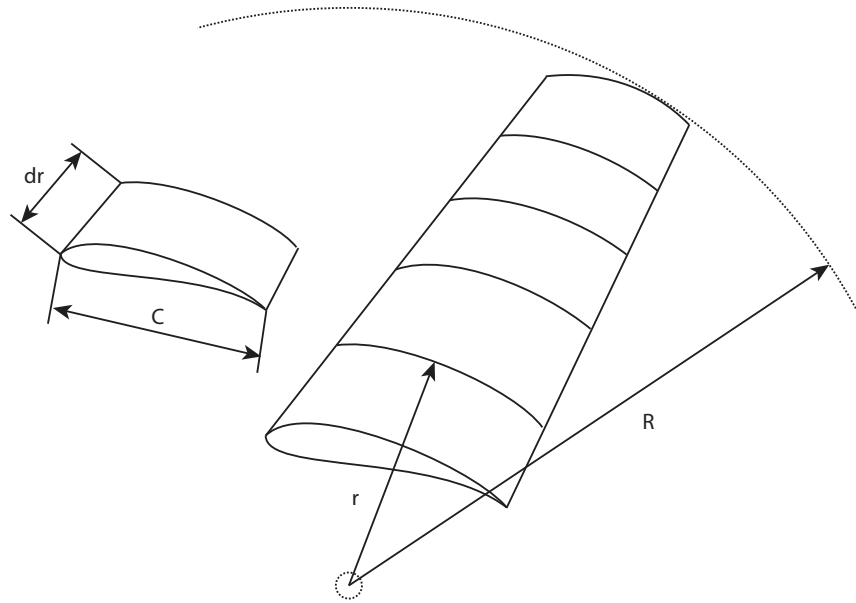


Figure 2-3: Schematic of blade elements

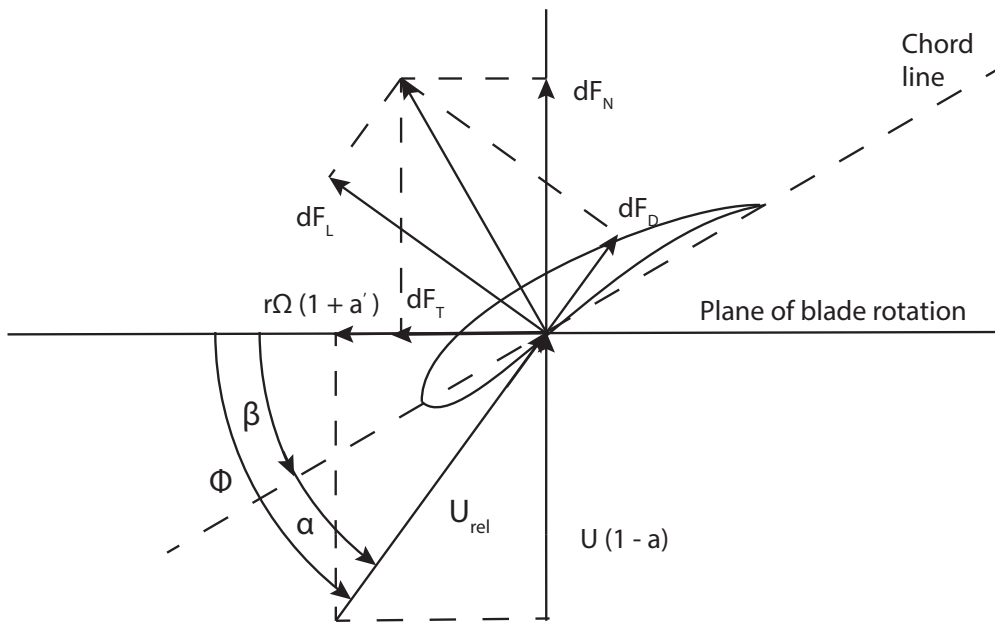


Figure 2-4: Local element geometry and forces

2D Model of Wave and Current Flow

As mentioned in the introduction chapter, the oscillating feature of waves will be modeled as a sinusoid curve. The simplest approach in the wave theory is the Airy linear wave model that will be explained in section 3-1. Then, the real sea states can be selected according to the local marine energy potential as well as the applicability of the Airy theory.

3-1 Airy linear wave model

The linear wave theory is the simplest wave model, and applicable only within the deep water region. To define the different water region, the classification of waves will firstly be introduced. An oscillatory wave can be characterized by the parameters shown in Fig. 3-1; those are height, H (distance from crest to trough), wavelength, L (distance between adjacent crests), the free surface elevation, η , period, T_w , and the still water depth, d .

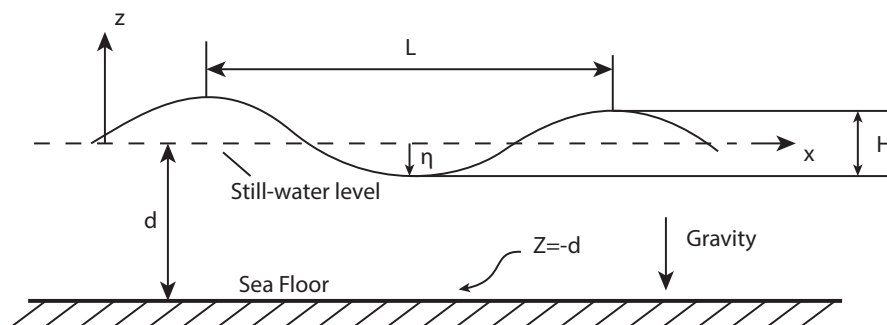


Figure 3-1: Characteristic measures for an oscillatory wave[2]

When d is small in comparison to L , the wave is classified as a shallow water wave. If the situation is the reverse, it is defined as a deep water wave. The wave types classified by the

key parameter d/L are summarized in Table. 3-1.

Classification	d/L
Deep	>0.5
Transitional	0.05 to 0.5
Shallow	<0.05
Very shallow	$\ll 0.05$

Table 3-1: Classification of wave types[2]

In deep water regions with small wave steepness, H/L , the most frequent solution is the Airy theory or linear wave theory because of its simplicity. The governing equations are derived from the potential flow theory and work with a 2-dimensional Cartesian coordinate in x and z directions (see Fig. 3-1) [2]. The origin of the x - z reference frame is located at the still water level with x aligned with the wave propagation direction and gravity is assumed to act in the negative z direction. According to Airy, the water particle follows an elliptical path with the major axis oriented along x -axis. When it comes to deep water, the influence from the seabed diminishes, and then the particle orbits tend toward circles[2]. The particle motion is shown in Fig. 3-2.

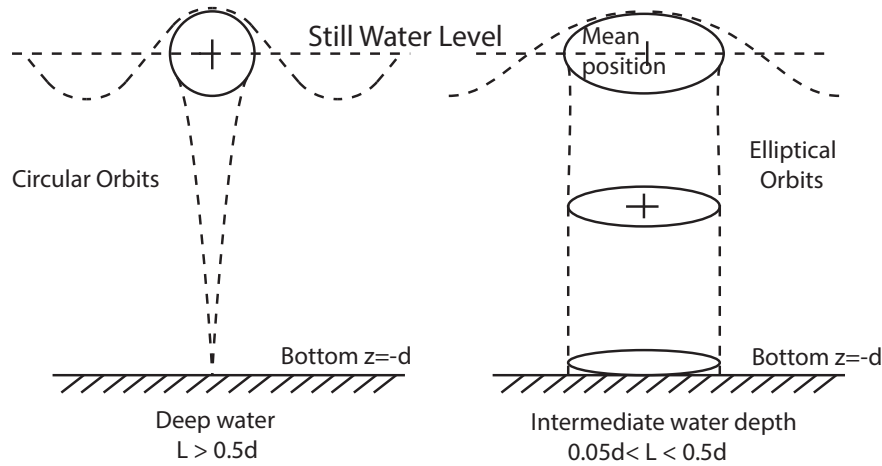


Figure 3-2: Particle orbits according to the Airy theory[3]

Based on the above assumption, Airy theory neglects the nonlinear terms in the governing equations and describes the kinematics of the water particles by the following equations [2].

$$\eta = \frac{H}{2} \cos(kx - \omega t) \quad (3-1)$$

$$V_x = \frac{\pi H}{T_w} \frac{\cosh[k(z+d)]}{\sinh(kd)} \cos(kx - \omega t) \quad (3-2)$$

$$V_z = \frac{\pi H}{T_w} \frac{\sinh[k(z+d)]}{\sinh(kd)} \sin(kx - \omega t) \quad (3-3)$$

with g is the gravitational acceleration, ω is the circular frequency ($\omega = 2\pi/T_w$) and k is the wave number. k and ω are related by the dispersion equation [2]:

$$\omega^2 = gk \cdot \tanh(kd) \quad (3-4)$$

Then, the wave length, L and the velocity of propagation, C can be described as [2]:

$$L = \frac{2\pi}{k}, \quad C = \frac{L}{T_w} = \frac{\omega}{k} \quad (3-5)$$

Eq. 3-3 gives the velocity variation on the z direction. However, in our study, the turbine will only consider the velocity on x direction. For the horizontal axis marine turbine, the actuator disk will be taken at the depth where the rotor axis lies. The z velocity at this depth is therefore fixed at a certain time; but it will be neglected in the study. Thus, only the Eq. 3-2 will be applied to calculate the velocity on x direction as the unsteady component of the income flow field velocity.

3-2 Scales of currents and waves

The sea area along the coastline of the UK is the choice for the scale selection. It is stated that the domestic tidal energy of the UK is around half of the European resource and about 10-15 % of the known global resource [15]. Large effort has been put into the assessment of extractable resource distribution and the relevant data are conveniently accessible through internet. The following wave and tide scales are based on the Atlas of the UK marine renewable energy resources [16]. The atlas contain information of tide, wave and wind resources. With region selection on the online map, one can easily get the water depth, tide speed, wave height and other relevant data. The maps [17] that show the bathymetry and the general resource information are also available and will be taken as the main reference for the estimation of the wave and tide scales.

As can be seen from Eq. 3-2, the wave velocity is modeled as a sinusoid curve. The amplitude of the velocity is determined by several parameters and some of them have inner relations. Whereas, the tidal current can be simply modeled with a constant as the income flow velocity. Thus, the wave resource will be studied first to set reasonable parameters.

The online atlas only give the significant height of the waves, H_s ; while the wave period can be derived from it. In real sea state, the relation between wave height and period is quite random. However, estimation can be made from analytical approximation [2]:

$$H_s = 0.115T_w^{1.788} \quad (3-6)$$

It is reported that about 50 % of the tide resource in the UK is in deep (>40m) sites and the flow velocities are quite high (>2.5 m/s) [15]. However, this will only provide the case

in which the tide flow is dominant. To obtain the different scales, a medium depth is taken here, $d = 30m$. Viewing from the map [17], areas with this water depth are featured with an annual mean significant wave height (H_s) of about 2m. Thus, the other wave parameters can be derived from Eq. 3-4 to Eq. 3-6; and the ratio between the water depth and the wavelength length (d/L) is calculated as around 0.77. From Table. 3-1, the Airy linear theory is valid in these regions.

With the chosen wave parameters, the amplitude of the velocity on x direction, $AmpV$, is now a function of the elevation, z :

$$AmpV = \frac{\pi H}{T_w} \frac{\cosh[k(z + d)]}{\sinh(kd)} \quad (3-7)$$

It can be seen from the curve (Fig. 3-3) of the above equation that the velocity amplitude decreases with the drop of the elevation.

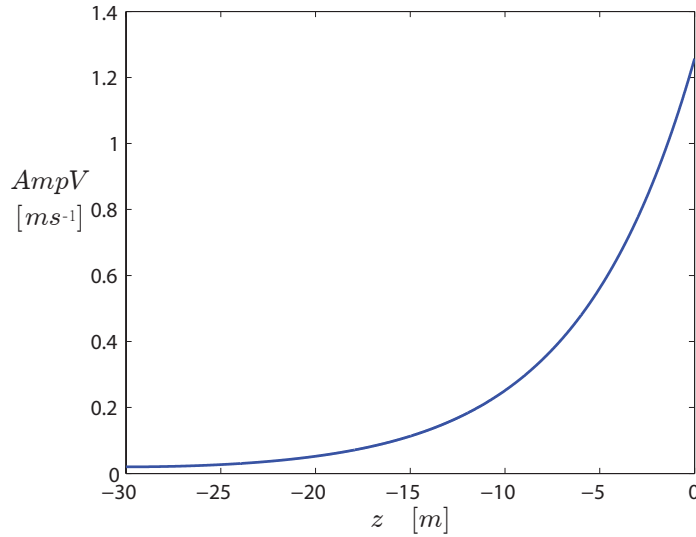


Figure 3-3: X velocity amplitude ($AmpV$) VS elevation (Z)

This can be physically explained by that the friction from the sea bottom diminishes the water movement [2]. Thus, to extract more energy, it is better to put the turbine closer to the sea surface. In the measurement of tidal current resource, the velocity is often represented by the Mean Spring Peak Velocity, V_{msp} . It is the tidal flow velocity taken at 5m below the surface [15]. Therefore, to make the scale combination more realistic, for the wave velocity amplitude calculation, we also choose the elevation as $z = -5m$. An overview of the wave parameters used for the estimation of wave velocity amplitude is shown in Table. 3-2.

H_s	T_w	d	k	L	ω	C
2 m	5 s	30 m	0.16 m	39 m	1.26 rad/s	7.80 m/s

Table 3-2: Wave parameters

The amplitude is thus derived as $AmpV = 0.56$. It should be noted that the wave period in Table. 3-2 is just a primary value for the amplitude estimation. To further study the relationship between period, T_w , and the velocity amplitude, $AmpV$, we vary the period within a reasonable range. Table. 3-3 shows the wave velocity amplitudes based on different T_w values.

T_w [s]	$AmpV$ [m/s]
5	0.56
6	0.6
7	0.6
8	0.59
9	0.59
10	0.59

Table 3-3: Wave period VS Amplitude of the wave velocity

It can be summarized from Table. 3-3 that within the range of 5-10 s (which is the typical wave period range of the North Sea [18]), the wave period has little influence on the velocity amplitude. Thus, in the model, $AmpV$ is assumed to be independent from the period and is chosen as $AmpV = 0.6m/s$.

With the fixed amplitude of wave velocity as the baseline, the current flow velocities (V_c) are chosen for different cases. According to the maps of the local bathymetry and the corresponding tidal current resources [15], the current velocities in the area of 30 m water depth rang from <0.11 m/s to >3 m/s. It is assumed that in the first scale, there will be zero current flow velocity. Thus, the output will show how the rotor behaves in a pure oscillating flow. Scale 2 represents the combination in which the wave velocity slightly dominants while Scale 4 reverses. The situation in which these two values are equal will be modeled by Scale 3. At last, Scale 5 will show the outputs under the circumstance that the current velocity is much larger than the wave. The values of the real sea states chosen for the different scales are shown in Table. 3-4.

Scale Number	$ALPHA = \frac{AmpV}{V_c}$	$AmpV$ [m/s]	V_c [m/s]
1	-	0.6	0
2	2	0.6	0.3
3	1	0.6	0.6
4	0.5	0.6	1.2
5	0.2	0.6	3

Table 3-4: Scales with different wave and tidal velocity combination from real sea states

The sum of the wave and current will result in an income flow with a sinusoid shape of which the mean value is the current velocity and the amplitude equals that of the wave velocity. Since the wave velocity is always varying, we will set the average value of the income flow velocity, the current velocity, as the reference velocity for the parameter evaluation. Thus, in the modeling, the current velocity is set as 1. With the ratio between $AmpV$ and V_c ,

$ALPHA = AmpV/V_c$, the scales for different wave and current combinations applied in the coding are listed in Table. 3-5. The income flow velocity is thus defined as:

$$U = V_c + ALPHA \cdot \cos(kx - \omega t) \quad (3-8)$$

Case Number	V_c [m/s]	$ALPHA$
1	1	0
2	1	0.2
3	1	0.5
4	1	1
5	1	2
6	0	1

Table 3-5: Scales with different wave and tidal velocity combination for modeling

with Case 1 and 6 are the two extreme situations: only current and only wave.

The model will then simulate these scales under two different operation conditions. One is to run the turbine with constant force applied on the rotor disk, which points to the negative x direction; in the other situation, the thrust coefficient is specified and the thrust on the disk is then computed from:

$$T = \frac{1}{2} C_T \rho A U^2 \quad (3-9)$$

Eq. 3-9 gives the magnitude of the thrust which is proportional to U^2 ; while the direction of the thrust force is always pointing against the income flow velocity.

Unsteady Actuator Disk Model

The BEM theory introduced in Chapter 2 is one of the most commonly used methods for the wind turbine studies because of its simplicity. However, it does have limitations and the main one that limits its application in our study case is that the calculations of BEM are static. To observe the turbine's responses from the unsteady input flows, the unsteady actuator disk model is utilized in our case.

4-1 Unsteady free-wake vortex method

In the free wake vortex method, the velocities at the rotor is calculated from the wake induction. The rotor here is still treated as the classical 2D actuator disk with a uniform, normal load distribution. Thus, the variation of the load on the disk will only occur at the edge with an infinite radial gradient. The derivation of the vortex generation from the force gradient is explicitly explained in van Kuik's work [4] and will be briefly introduced here.

According to the basic assumptions of the actuator disk model (Section 2-1), the fluid is considered as incompressible, homogeneous and inviscid; therefore, the Euler equation is valid:

$$\rho \frac{D\mathbf{v}}{Dt} = -\nabla p + \mathbf{f} \quad (4-1)$$

together with the continuity equation:

$$\nabla \cdot \mathbf{v} = 0 \quad (4-2)$$

with \mathbf{v} is the velocity vector, p is the static pressure and \mathbf{f} is the force density distribution. With the Bernoulli constant, $H = p + \frac{1}{2}\rho\mathbf{v} \cdot \mathbf{v}$ and the vorticity, $\boldsymbol{\omega} = \nabla \times \mathbf{v}$, Eq. 4-1 is reshaped as:

$$\nabla H = \mathbf{f} + \rho\mathbf{v} \times \boldsymbol{\omega} - \rho \frac{\partial \mathbf{v}}{\partial t} \quad (4-3)$$

By taking curl of the both sides of Eq. 4-3, in 2D flow case, it gives:

$$\frac{1}{\rho} \nabla \times \mathbf{f} = \frac{\partial \omega}{\partial t} + (\mathbf{v} \cdot \nabla) \omega = \frac{D\omega}{Dt} \quad (4-4)$$

This illustrates that the generation of the vorticity only depends on $\nabla \times \mathbf{f}$. Fig. 4-1 gives a view of the cross section through an actuator surface [4].

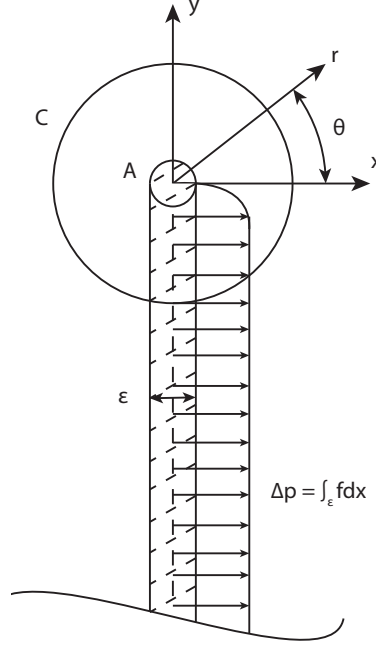


Figure 4-1: Cross-section through an actuator surface[4]

Since the integration of \mathbf{f} on x-component is the pressure jump, $\nabla p = \int f dx$, the integration of $\nabla \times \mathbf{f}$ across the thickness ϵ yields:

$$\mathbf{e}_z \cdot \int_{\epsilon} \nabla \times \mathbf{f} dx = - \int \frac{df}{dy} dx = - \frac{d\Delta p}{dy} \quad (4-5)$$

With Stoke's theorem, the integration of $\nabla \times \mathbf{f}$ on the edge area A equals:

$$\mathbf{e}_z \cdot \iint_A \nabla \times \mathbf{f} dA = \oint_C f dc = \Delta p \quad (4-6)$$

with C is a contour that encloses the area A. Substitute this into Eq. 4-4 yields:

$$\mathbf{e}_z \cdot \iint_A \frac{D\omega}{Dt} dA = \frac{D\Gamma}{Dt} = \frac{\Delta p}{\rho} \quad (4-7)$$

Now, the numerical method treats the vortex generated at the disc tip as a vortex blob. The vortex shedding process of the 2D actuator disk is shown in Fig. 4-2. At each time step, Δt ,

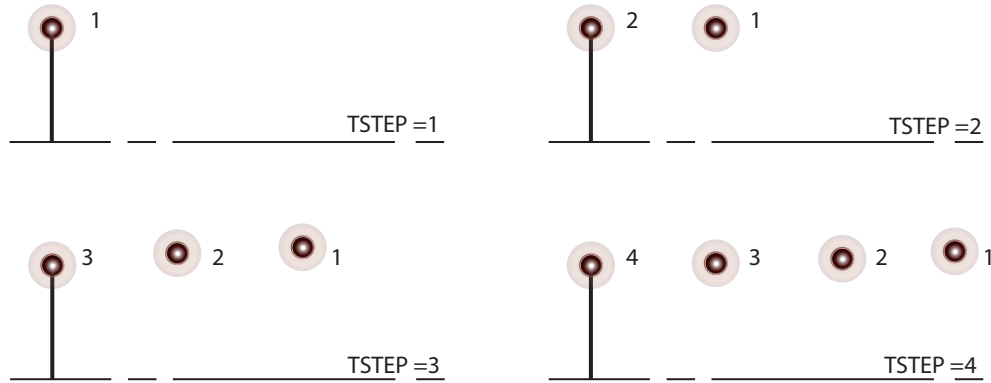


Figure 4-2: Vortex shedding process

a new vortex blob will be generated from the tips with the circulation strength[19]:

$$\Gamma = \frac{\Delta p}{\rho} \Delta t \quad (4-8)$$

From the momentum theory, the pressure difference is calculated from:

$$\Delta p = \frac{1}{2} \rho U^2 C_T \quad (4-9)$$

with: C_T : thrust coefficient

These blobs are then shed into the wake traveling with a resultant speed determined by the income flow velocity, \mathbf{U} (in our case, the velocity is only on x direction) and the induced velocity from other blobs, \mathbf{V} .

$$\mathbf{V}_{res}(i) = \mathbf{U} + \sum_{j \neq i}^N \mathbf{V}(i, j) \quad (4-10)$$

with N is the number of the vortices released, which is equal to the number of the time steps, $TSTEP$.

In a 2D Cartesian coordinate, for an arbitrary location (x_i, y_i) , the velocities induced by a vortex located at (x_j, y_j) are computed as:

$$\begin{aligned} u(i, j) &= \frac{\Gamma}{2\pi} \frac{y_j - y_i}{(y_j - y_i)^2 + (x_j - x_i)^2} \\ v(i, j) &= -\frac{\Gamma}{2\pi} \frac{x_j - x_i}{(y_j - y_i)^2 + (x_j - x_i)^2} \end{aligned} \quad (4-11)$$

Then, the resultant velocities for an individual vortex in the 2D coordinate are:

$$\begin{aligned}
V_x(i) &= U + \sum_{j \neq i}^N u(i, j) \\
V_y(i) &= \sum_{j \neq i}^N v(i, j)
\end{aligned} \tag{4-12}$$

Thus, for the next time step, the existing vortices will travel a distance by:

$$\begin{aligned}
\Delta x(i) &= V_x(i)_{t-1} \Delta t \\
\Delta y(i) &= V_y(i)_{t-1} \Delta t
\end{aligned} \tag{4-13}$$

With the geometry of the vortices in the wake, the fluid velocity at any point of the 2D flow field is then computed as the sum of the undisturbed income stream velocity and the velocity induced by all the vortices.

4-2 Runge-Kutta Method

To refine the numerical computation, the iterative method is applied to the unsteady actuator disk model. The specific method applied here is the fourth-order Runge-Kutta method which is often referred to as "RK4". Instead of a general description, the RK 4 will be introduced here with the integration of the original model. The following equations are based on the formulation presented in Atkinson's book [20].

As illustrated in the previous section, the vortex traveling velocity is a function of time and the position:

$$(V_x, V_y) = f(t, (x, y)) \tag{4-14}$$

with the position (x, y) is an unknown function of time. Here, the initial values of the problem are given as $t_0, (x_0, y_0)$. When the time step number is n , we pick a vortex which travels with an instantaneous velocity, (V_{nx}, V_{ny}) . RK 4 then gives the position of this vortex for next time step number $(n + 1)$ as:

$$\begin{aligned}
(x_{n+1}, y_{n+1}) &= (x_n, y_n) + \frac{1}{6} \Delta t ((k_{1x}, k_{1y}) + 2(k_{2x}, k_{2y}) + 2(k_{3x}, k_{3y}) + (k_{4x}, k_{4y})) \\
t_{n+1} &= t_n
\end{aligned} \tag{4-15}$$

with $k_1(k_{1x}, k_{1y}), k_2(k_{2x}, k_{2y}), k_3(k_{3x}, k_{3y}), k_4(k_{4x}, k_{4y})$ are defined as:

$$\begin{aligned}
(k_{1x}, k_{1y}) &= f(t_n, (x_n, y_n)), \\
(k_{2x}, k_{2y}) &= f\left(t_n + \frac{1}{2}\Delta t, (x_n, y_n) + \frac{\Delta t}{2}(k_{1x}, k_{1y})\right), \\
(k_{3x}, k_{3y}) &= f\left(t_n + \frac{1}{2}\Delta t, (x_n, y_n) + \frac{\Delta t}{2}(k_{2x}, k_{2y})\right), \\
(k_{4x}, k_{4y}) &= f(t_n + \Delta t, (x_n, y_n) + \Delta t(k_{3x}, k_{3y})).
\end{aligned} \tag{4-16}$$

(k_{1x}, k_{1y}) equals the velocity, (V_{nx}, V_{ny}) , which is the rate of the position change at the beginning of the time step. In the original model, the vortex traveling distance is directly computed from the product of (V_{nx}, V_{ny}) and the time interval, Δt (Eq. 4-13). In RK4, k_2 and k_3 take the rate at the midpoint of the interval into calculation while k_4 considers the endpoint change rate. Thus, it leads to a more accurate approximation to the real position change.

2D Potential Flow Panel Method (VAT)

For the modeling of VAT in the wave current flow, the 2D panel code developed by C. Simão. Ferreira [14] is applied here. The integration of the income flow condition to the panel code is done by modifying the income wind script profile according to the wave model introduced in Section 3-1. The original panel code is based on the unsteady formulation explained by Katz and Plotkin [21]. Here, we will introduce the panel method following the numerical solution steps recommended by Katz and Plotkin with some specific simulation data involved in the 2D panel code.

5-1 Selecting the singularity element

For the potential flow, the panel (numerical) method can be briefly summarized as dividing the problem surface (e.g. airfoil surface) into piecewise straight line segments or panels and then finding the strength of the singularity elements distributed on the surface [21]. The first step is to choose the singularity elements that will be used. The usual options are sources, σ , doublets, μ , and vortices, Γ , or any combination of them. These basic singularity solutions of the potential flow are explicitly explained in the work of Katz and Plotkin with the computation of the relevant induced velocity and potential.

In the panel code applied here, a combination of sources and doublets is distributed on the airfoil. The near-wake is then represented with doublets while the mid and far wake are modeled with vortex points.

5-2 Discretizing the geometry

This step generates the grid of the problem surface by dividing the geometry into panels and thus defines the corner points and collocation (control) points for each segment. The collocation points are the locations where the boundary conditions need to be fulfilled. Two boundary conditions or their combination can be chosen for the building of the numerical calculation, the Neumann boundary condition and the Dirichlet boundary condition. In the case of Neumann, the collocation points are selected on the surface and the zero normal velocity condition need to be satisfied directly:

$$\nabla(\Phi + \Phi_\infty) \cdot \mathbf{n} = 0 \quad (5-1)$$

with Φ_∞ is the free-stream potential and Φ is the perturbation potential. The total potential is defined as the sum of these two: $\Phi^* = \Phi + \Phi_\infty$.

The Dirichlet boundary condition indirectly meets the zero normal velocity requirement by setting the potential inside the body, Φ_i^* , as a constant.

$$\Phi_i^* = const. \quad (5-2)$$

Therefore, in Dirichlet case, the control points need to be placed inside the surface.

The 2D panel code here sets up the Dirichlet boundary condition for the calculation. The airfoil chosen for the rotor model is a NACA0015 which is then subdivided into 190 panels. The control points are placed slightly inside the airfoil and at the middle of each panel.

5-3 Determining the influence coefficients and establishing the system of equations

The establishment of the influence coefficient matrix is based on the previous steps. For the Dirichlet boundary condition chosen in the panel code, the calculation of the influence coefficients involves both the induced potential formulation and the collocation point geometry. The specific expression of the influence coefficient will not be included here. Instead, we simply represent the coefficient of source element as a_{ij} .

For the doublets, an additional wake panel, μ_w , need to be added to fulfill the Kutta condition that the circulation at the trailing edge is zero:

$$(\mu_1 - \mu_N) + \mu_w = 0 \quad (5-3)$$

with μ_1 and μ_N are the doublets of the first and the N^{th} panel. It will then result in $N + 1$ linear equations:

$$\sum_{i=1}^{N+1} \sum_{j=1}^{N+1} C_{ij} \mu_j = \begin{pmatrix} c_{11} & c_{12} & \cdots & \cdots & c_{1N} & c_{1w} \\ c_{21} & c_{22} & \cdots & \cdots & c_{2N} & c_{2w} \\ \cdots & \cdots & \cdots & \cdots & \cdots & \cdots \\ c_{N1} & c_{N2} & \cdots & \cdots & c_{NN} & c_{Nw} \\ 1 & 0 & 0 & \cdots & -1 & 1 \end{pmatrix} \begin{pmatrix} \mu_1 \\ \mu_2 \\ \cdots \\ \mu_N \\ \mu_w \end{pmatrix} \quad (5-4)$$

Substitute μ_w with Eq. 5-3 and reshape the above matrix into $N \times N$ size. Rewrite the doublet influence coefficients as:

$$\begin{aligned} b_{ij} &= c_{ij} & j &\neq 1, N \\ b_{i1} &= c_{i1} - c_{iw} & j &= 1 \\ b_{iN} &= c_{iN} + c_{iw} & j &= N \end{aligned} \quad (5-5)$$

Now, for every collocation point, the matrix equation will be:

$$\begin{pmatrix} a_{11} & a_{12} & \cdots & a_{1N} \\ a_{21} & a_{22} & \cdots & a_{2N} \\ \cdots & \cdots & \cdots & \cdots \\ \cdots & \cdots & \cdots & \cdots \\ a_{N1} & a_{N2} & \cdots & a_{NN} \end{pmatrix} \begin{pmatrix} \sigma_1 \\ \sigma_2 \\ \cdots \\ \sigma_N \end{pmatrix} + \begin{pmatrix} b_{11} & b_{12} & \cdots & b_{1N} \\ b_{21} & b_{22} & \cdots & b_{2N} \\ \cdots & \cdots & \cdots & \cdots \\ \cdots & \cdots & \cdots & \cdots \\ b_{N1} & b_{N2} & \cdots & b_{NN} \end{pmatrix} \begin{pmatrix} \mu_1 \\ \mu_2 \\ \cdots \\ \mu_N \end{pmatrix} = 0 \quad (5-6)$$

In the panel code, the source strength is specified to be the total potential that the element will perceive. It is thus the sum of the potential due to the income flow, the wake and the movement of the airfoil during the rotation. Then, with the source, σ known, the Right-Hand Side (RHS) is:

$$\begin{pmatrix} RHS_1 \\ RHS_2 \\ \cdots \\ \cdots \\ RHS_N \end{pmatrix} = - \begin{pmatrix} a_{11} & a_{12} & \cdots & a_{1N} \\ a_{21} & a_{22} & \cdots & a_{2N} \\ \cdots & \cdots & \cdots & \cdots \\ \cdots & \cdots & \cdots & \cdots \\ a_{N1} & a_{N2} & \cdots & a_{NN} \end{pmatrix} \begin{pmatrix} \sigma_1 \\ \sigma_2 \\ \cdots \\ \cdots \\ \sigma_N \end{pmatrix} \quad (5-7)$$

5-4 Solving linear set of equations and secondary computing

Now, the doublets can be solved from the linear set of equations:

$$\begin{pmatrix} b_{11} & b_{12} & \cdots & b_{1N} \\ b_{21} & b_{22} & \cdots & b_{2N} \\ \cdots & \cdots & \cdots & \cdots \\ \cdots & \cdots & \cdots & \cdots \\ b_{N1} & b_{N2} & \cdots & b_{NN} \end{pmatrix} \begin{pmatrix} \mu_1 \\ \mu_2 \\ \cdots \\ \cdots \\ \mu_N \end{pmatrix} = \begin{pmatrix} RHS_1 \\ RHS_2 \\ \cdots \\ \cdots \\ RHS_N \end{pmatrix} \quad (5-8)$$

Once the doublet strength μ_j is known, the local external tangential velocity above each control point is calculated as the differentiation of the velocity potential along the tangential direction and the simplest numerical interpretation is:

$$U_{t_j} = \frac{\mu_{j+1} - \mu_j}{\Delta l_j} + U_{t_\infty} \quad (5-9)$$

with Δl_j is the distance between the two adjacent control points. U_{t_∞} here is the sum of the tangential component of the income flow velocity and the velocity due to the movement of the airfoil. In the 2D panel code, a time derivation of the doublets is applied to refine the computation. Thus, with the reference income flow velocity set as $U_{ref} = 1$, the pressure coefficient can be computed by Eq. 5-10:

$$C_{P_j} = 1 - \frac{U_{t_j}^2}{U_{ref}^2} - 2 \frac{D\mu/Dt}{U_{ref}^2} \quad (5-10)$$

Then the contribution to the force coefficient distributed on the X direction and Y direction are:

$$\begin{aligned} \Delta C_{Fx_j} &= -C_{P_j} \Delta l_j \mathbf{e}_x \\ \Delta C_{Fy_j} &= -C_{P_j} \Delta l_j \mathbf{e}_y \end{aligned} \quad (5-11)$$

The total force on each direction is obtained by summing the force on each element:

$$\begin{aligned} C_{Fx_j} &= \sum_{j=1}^N \Delta C_{Fx_j} \\ C_{Fy_j} &= \sum_{j=1}^N \Delta C_{Fy_j} \end{aligned} \quad (5-12)$$

The simulation process is similar to the free wake model in Section 4-1. For each time step, the airfoil rotates to a new position. The control points on the airfoil will then perceive new income flow velocities which are determined by both the simulation time and the coordinates of the points. At the mean time, the previous wake will travel to a new geometry. With the updated income flow and wake information, the source and doublets distribution will be calculated following the steps above. The result will then lead to the new vortex shedding from the trailing edge to the wake.

Recalling Eq. 4-13, for each time step, the traveling distance of the existing vortex is determined by the previous resultant velocity of the vortex. However, for the simulation convenience, in the coding, the traveling velocity is taken as the new velocity at the current time step. Since there is inherent deviation involved in the numerical computation due to the assumption that within the small time step, the relevant properties remain unchanged, the error here is then treated as acceptable.

Simulations for Different Wave Current Cases - 2D Actuator Disk

This chapter discusses the results from the 2D unsteady actuator disk model. As explained in Chapter 3, Case 1 to 6 in Table. 3-5 are simulated individually. The corresponding wake geometry and the induction factor, a , are presented here. For the calculation of a , we choose the current velocity as the reference velocity, thus, a is defined as:

$$a = -u_{disk}/V_c \quad (6-1)$$

with u_{disk} is the induced velocity at the disk center which is computed from Eq. 4-11. The reason that we choose V_c instead of the instantaneous income flow velocity (U) is due to the phase delay observed between U and the u_{disk} , which means, the induction factor based on U can be infinite when $U = 0$ in some cases. The following sections will discuss the results from each case separately.

6-1 The current case - baseline actuator disk

In the first case here, only the current velocity is involved, which means it is a case of steady flow. It can be seen from Fig. 6-1, vortices are shedding behind the rotor disk. After several time steps ($TSTEP$), the tail of the wake starts to roll up. With large amount of vortices shed into the wake (in our case, $TSTEP \geq 1000$), the wake will finally reach a steady state. The induced velocity at the disk center, u_{disk} , and the induction factor will also approach steady.

Comparison with BEM

From BEM, the relationship between induction factor and the thrust coefficient is $C_T = 4a(1 - a)$. To validate the free wake vortex model by comparing with BEM, we vary C_T

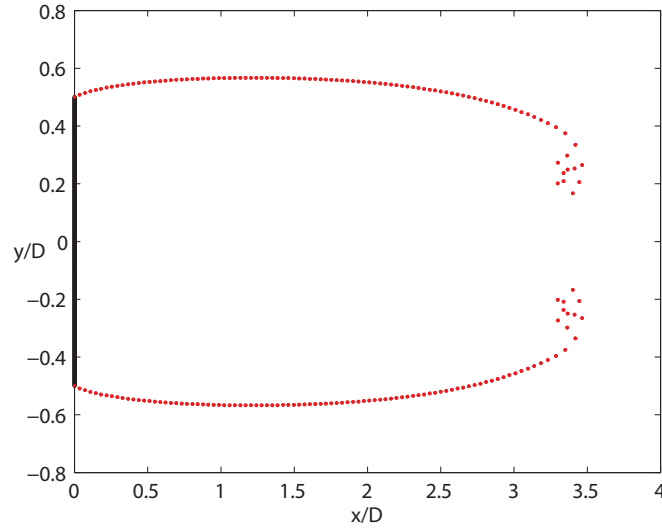


Figure 6-1: Wake Geometry of the current case at TSTEP = 100

from 0 – 1 to observe the output values of the induction factor. The corresponding results from BEM and the free wake vortex model are described in Fig. 6-2. From the figure, we can see that these two models match well in the low load region while the difference can be found in the high load region, especially for the area where a exceeds the Betz limit, $a = \frac{1}{3}$. One cause for the difference is that the BEM theory becomes invalid where $a > \frac{1}{3}$ [22]. The other is probably due to the inherent deviation of the numerical computation method. The Glauert correction is recommended for the validation of the high load case. However, in our research, we just choose the low load situation for the simulation. The red point in Fig. 6-2 is the thrust coefficient applied in the simulation: $C_T = 0.65$ and the corresponding theoretical induction factor given by BEM is $a = 0.204$.

6-2 Wave case

The above section shows that the constant current velocity finally leads to a steady state which matches well with the BEM prediction. Now the cases with pure wave oscillation will be studied, which is further sub-divided into two operation conditions: constant force and varying force applied on the rotor disk.

6-2-1 Wave case - constant force

In this case, the rotor is assumed to be operated with a constant force pointing to the negative x -direction. Recalling Eq. 3-9, the constant force here is computed by replacing the income flow velocity by a reference velocity $U_{ref} = 1$. The force distributed on the rotor disk per unit area with non-dimensionalization by diving the fluid density is then:

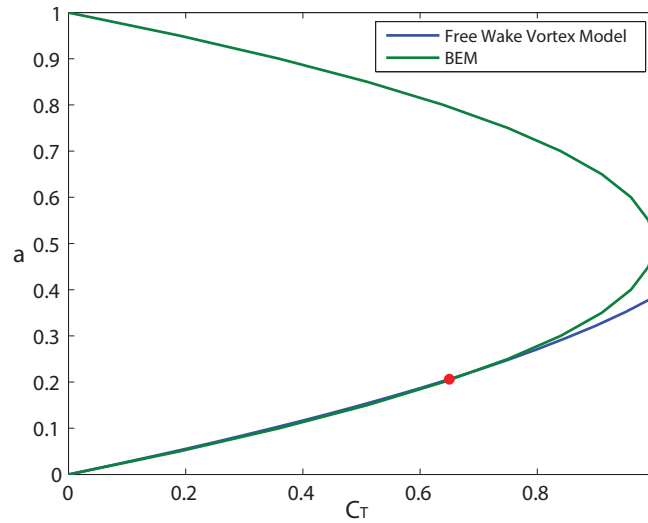


Figure 6-2: Comparison of the induction factor from BEM and the free wake vortex model

$$f_{Tconst} = \frac{1}{2} C_T U_{ref}^2 \quad (6-2)$$

Vortices are then released from the tip. With the force keeping constant, the tip vortices shed at different time steps share the same circulation strength and direction. We then represent these vortices with red points in the geometry.

Fig. 6-3 shows the wave oscillation within one period, T_w . The red circle points are the four turning points, $N \cdot T_w$, $(N + 1/4) \cdot T_w$, $(N + 1/2) \cdot T_w$ and $(N + 3/4) \cdot T_w$ (N is an arbitrary integer). The wake geometry development process in one T_w at these four points is indicated in the following figures.

Fig. 6-4 to Fig 6-7 show that the vortices travel back and forth corresponding to the wave oscillation. However, the whole vortex group travel to the negative x direction. Recalling Eq. 4-12, without a dominant U in the positive x direction, the resultant velocity of the vortex is negative at most of the time since the induced velocity from other vortices is negative. The same thing happened at the disk center where the resultant velocity, $U_{res} = U + u_{disk}$, is mostly negative. While the thrust generated by the disk is pointing to the positive direction. Thus, the power output in this case is almost negative and the turbine is actually acting similar to a propeller.

6-2-2 Wave case - varying force

The variation of the force is defined in Chapter 3: the force is always pointing against the income flow velocity with the magnitude proportional to U^2 . Same as the non-dimensional

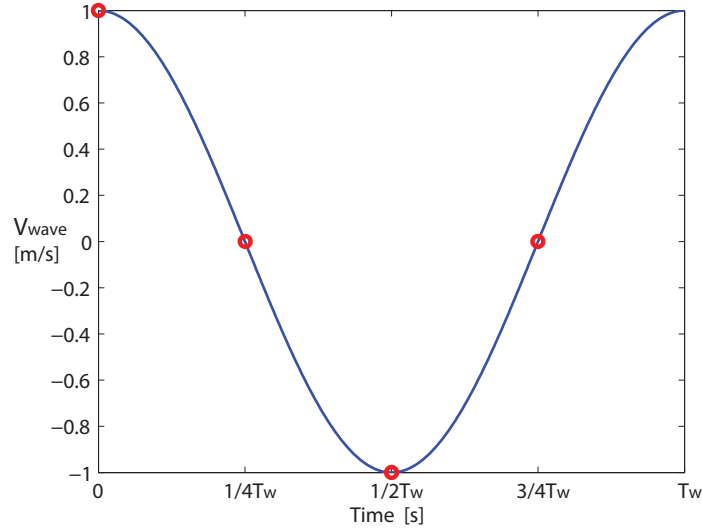


Figure 6-3: Wake velocity oscillation within a wave period

f_{Tconst} , the varying force distribution is then:

$$f_{Tvary} = \frac{1}{2} C_T U^2 \quad (6-3)$$

Now the vortices released from the tip vary not only in circulation strength but also in the direction. In the geometry graph, the red points represent the vortices which are released when the wave velocity is positive while the blue ones are opposite. It can be seen that the main part of the wake is shedding to the positive direction and the power output in this case is positive which is shown by the power coefficient (Fig. 6-9).

The power coefficient, C_P here is defined as:

$$C_P = \frac{P_{center}}{\frac{1}{2} U_{ref}^3} \quad (6-4)$$

with P_{center} is the power generated at the center of the disk, which is computed as:

$$P_{center} = f_{Tvary} \cdot U_{res} \quad (6-5)$$

Since the wave power computation in Eq. 1-2 gives an overall power, to trace the instantaneous variation of the power, the computation of C_P is then based on the reference velocity, $U_{ref} = 1$, as illustrated in the equations above.

The power output here is oscillating. Attention needs to be paid to some heavy variation parts on the curve. To further understand those abnormal variations, we then study the induced velocity at the center of the disk. Viewing from Fig. 6-10, the large variations also happen in the u_{disk} . By tracing the time when the variations occur, it is found that some vortices that

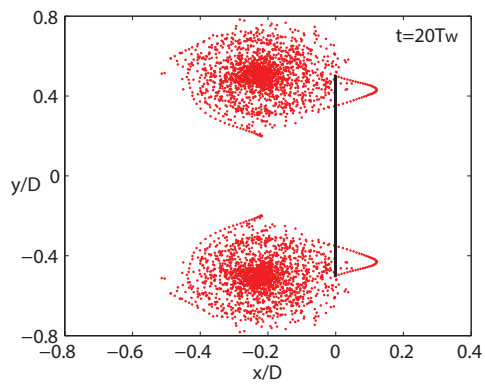


Figure 6-4: Wake geometry of wave case, constant force, $t = 20T_w$

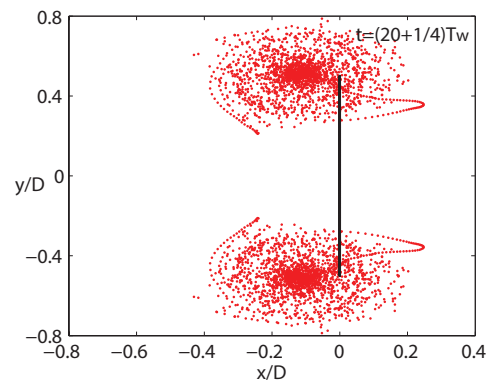


Figure 6-5: Wake geometry of wave case, constant force, $t = (20 + \frac{1}{4})T_w$

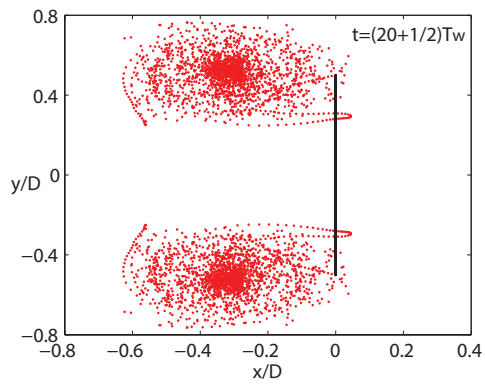


Figure 6-6: Wake geometry of wave case, constant force, $t = (20 + \frac{1}{2})T_w$

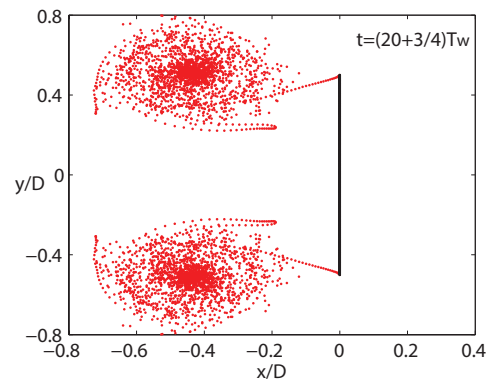


Figure 6-7: Wake geometry of wave case, constant force, $t = (20 + \frac{3}{4})T_w$

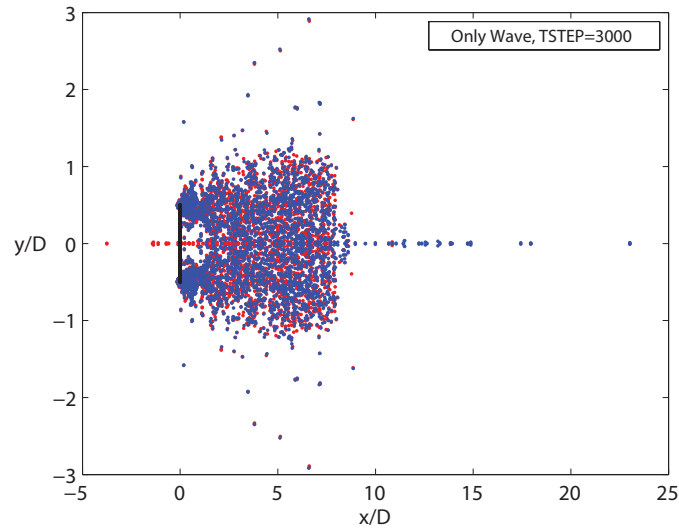


Figure 6-8: Wake geometry of the wave case with varying force

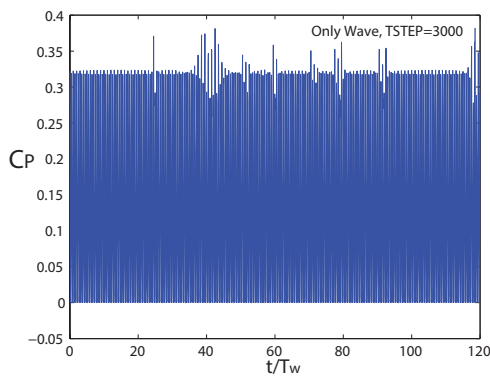


Figure 6-9: Power coefficient of the wave case with varying force

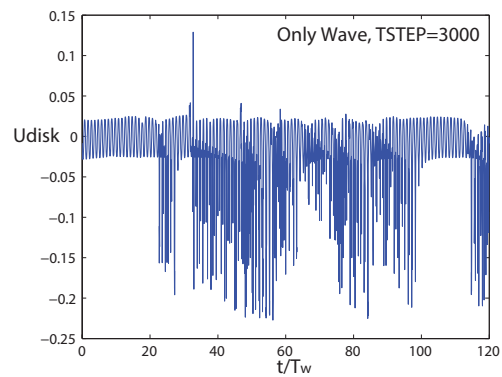


Figure 6-10: Induced velocity of the wave case with varying force

travel to the axis of the disk move back towards the disk. When they are crossing the disk, the self-velocities carried by those vortices bring the large variations.

Comparison with BEM

The results from these two operation conditions with only wave income flow indicate that they are inherently unsteady. In the two wave cases here, the BEM model does not give any useful information for comparison. Furthermore, since the result from the constant force case gives the negative power output while the result of varying force case indicates the risk of the heavy unsteady response from the disk. We may conclude that it is not recommended to apply the rotor disk to harvest energy from the pure wave flow.

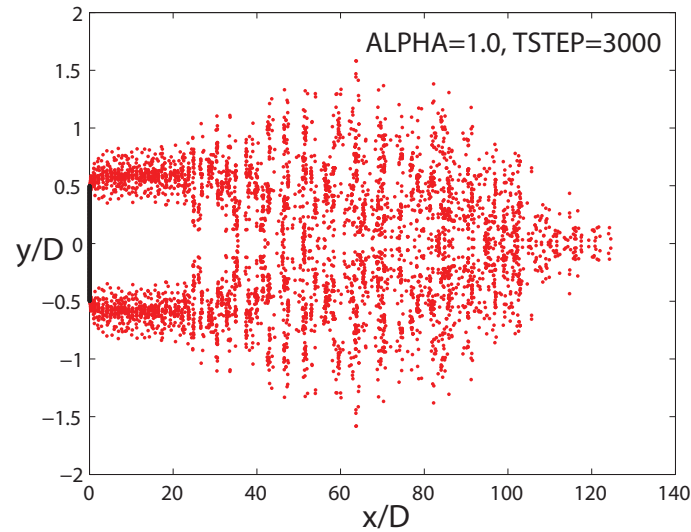


Figure 6-11: Wake geometry of the wave current case with constant force ($ALPHA = 1$)

6-3 Current and wave

After study the rotor behaviors in the wave and the current separately, now we start to integrate them with different scales. Same as the previous section, the operation condition is also categorized by the forces applied on the disk.

6-3-1 Current and wave - constant force

Different from the previous constant force, the force distribution here take the current velocity into computation ($f_{Tconst} = \frac{1}{2}C_T V_c^2$) since the mean value of the income flow velocity now equals V_c . From the simulation results, the wake geometry and the overall trend of the induction factor in Case 2 to Case 5 are similar. Thus, we only represent the Case 4 with $ALPHA = \frac{AmpV}{V_c} = 1$ for the discussion. The wake geometry and the induction factor are illustrated in Fig. 6-11 and Fig. 6-13.

With the integration of the current velocity pointing in the positive x -direction, for all the cases here, the dominant direction of the income flow velocity, U is positive. The vortices are then all shed to the back of the disk (positive x -direction). However, the power output is not always positive. For the Case 4 ($ALPHA = 1$) and Case 5 ($ALPHA = 2$), the negative C_P can be observed. Fig. 6-12 shows the power coefficient of Case 4 in the last period of the simulation time.

The definition of C_P is similar to the one defined in the wave case with only the U_{ref} replaced by V_c . We will first present the induction factor behavior which will then give an explanation for the occurrence of negative power.

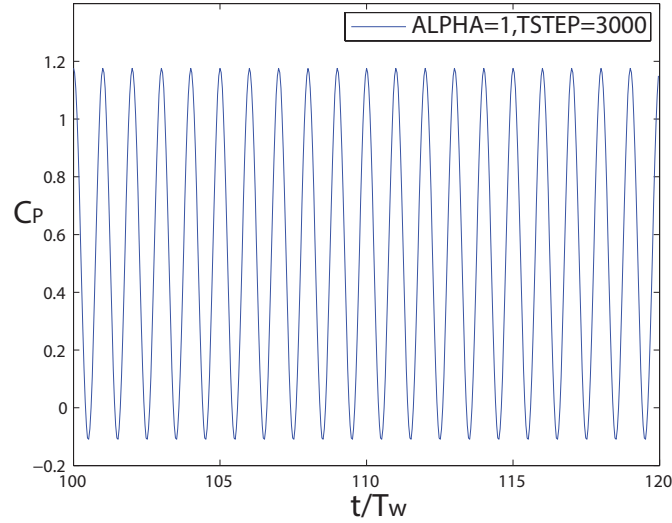


Figure 6-12: Power coefficient of the wave current case with constant force($ALPHA = 1$)

The corresponding induction factor in Fig. 6-13 finally reaches a periodic manner with the mean value, a_{mean} gradually approaches steady after a transition time. We then take the induction factor curve in the time period of the last time steps and try to fit it with a regular sinusoid curve. Fig. 6-14 shows the curve-fitting which matches well with the original curve. And from the equation of the sinusoid curve (for Case 4 here: $a = 0.0322 \cdot \sin(6.238(t/T_w) + 2.881)$), we can see that there exists a phase delay between a and the income flow velocity at the disk, U (Eq. 3-8). The induced velocity is always negative and when U is zero, the resultant velocity becomes less than zero which then leads to the negative power output. Until the current velocity takes a much more dominant place, the negative resultant velocity will disappear which guarantees a positive power output for all the time. Both in Case 2 and Case 3, the power coefficient is positive, however, the exact $ALPHA$ where the minimum power is zero is not studied here.

Comparison with BEM

Curve-fitting is applied for each case and the features are listed in Table. 6-1. It can be easily observed that the oscillating period of the induction factor equals the wave period. To further verify this conclusion, other cases with wave period from 3 s to 10s are also simulated and the results agree well with this observation.

Case	T_w [s]	V_c [m/s]	ALPHA ($AmpV/V_c$)	a_{mean}	T_a [s]
2	5	1	0.2	0.1974	5
3	5	1	0.5	0.1940	5
4	5	1	1	0.1853	5
5	5	1	2	0.1596	5

Table 6-1: Induction factor features of different wave current cases with constant force

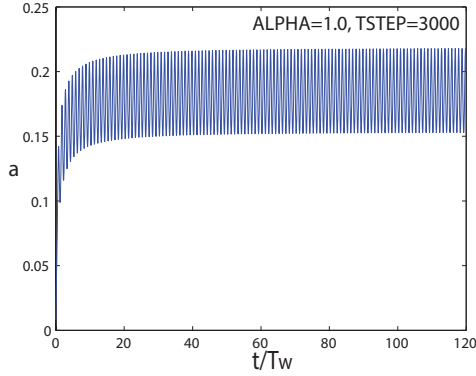


Figure 6-13: Induction factor of the wave current case with constant force ($ALPHA = 1$)

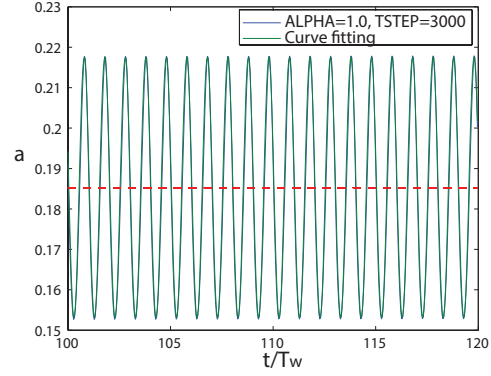


Figure 6-14: Curve-fitting for the induction factor for wave current case with constant force ($ALPHA = 1$)

In the Case 2 and Case 3, a_{mean} is near to the theoretical induction factor value given by BEM, $a = 0.204$. Considering the slightly increasing trend of a in Fig. 6-13, we may guess that even BEM fails in the prediction of the unsteady response, it may be helpful in the prediction of a_{mean} . With the limitation from the computation speed, the total time steps is set as 3000 for each case. Thus, this conclusion may be further verified by accelerating the model process and observing with a much larger $TSTEP$.

6-3-2 Current and wave - varying force

The case of varying force need to be discussed separately since the outputs from the situations where $ALPHA \leq 1$ are different from that of $ALPHA > 1$. When the current velocity is smaller than the wave velocity amplitude, here $ALPHA = 2$, vortices with negative circulation direction will be generated (represented in blue points). Fig. 6-15 to Fig. 6-19 show the vortex releasing process in one wave oscillating period. Similar to the case of varying force in the pure wave, the vortices gradually reach the axis of the disk and then will slightly travel back. In Fig. 6-20, the vortices have already reached the disk and started to cross the disk. The self velocities carried by those vortices will then cause the large variations in the response of the disk (t/T_w at around 100 in Fig. 6-21).

However, it is not clear yet whether the phenomenon that the vortices travel back to the disk will happen for all the cases where $ALPHA > 1$. Since when the ratio between V_c and $AmpV$ is close to 1, larger $TSTEP$ is required until the possible crossing can be observed.

When $V_c \geq AmpV$ ($ALPHA \leq 1$), the negative forces disappear. This situation is actually similar to the constant force. The difference is that the vortex circulations here have the same direction but varying magnitudes. The wake geometry and the induction factor turn out to behave in similar manners for Case 2 to Case 5. Thus, we also choose one example to present (Case 3, $Alpha = 0.5$) and the results are shown in Fig. 6-22 and Fig. 6-23.

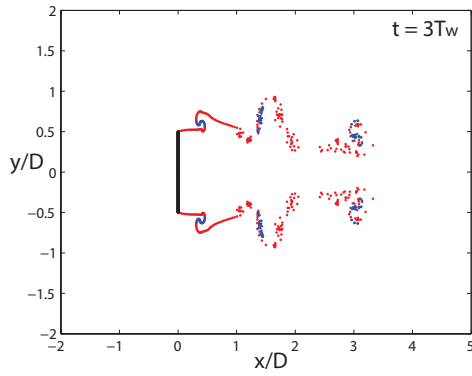


Figure 6-15: Wake geometry of wave current case with varying force ($ALPHA = 2, t = 3T_w$)

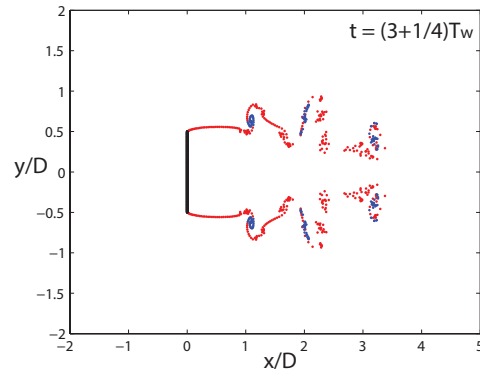


Figure 6-16: Wake geometry of wave current case with varying force ($ALPHA = 2, t = (3 + \frac{1}{4})T_w$)

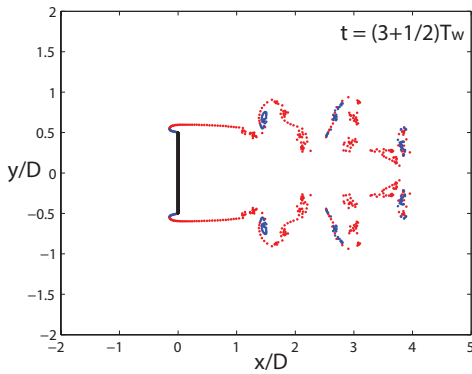


Figure 6-17: Wake geometry of wave current case with varying force ($ALPHA = 2, t = (3 + \frac{1}{2})T_w$)

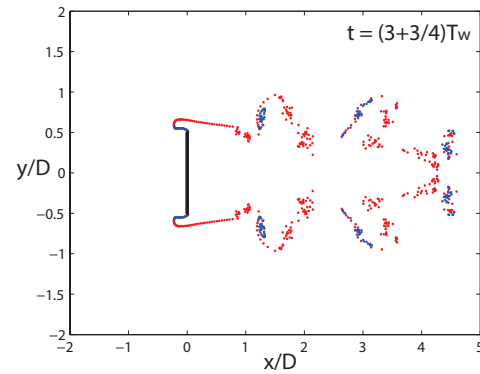


Figure 6-18: Wake geometry of wave current case with varying force ($ALPHA = 2, t = (3 + \frac{3}{4})T_w$)

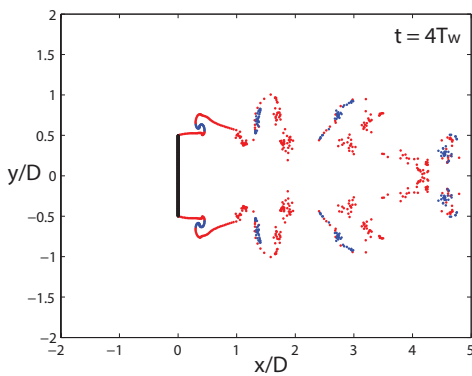


Figure 6-19: Wake geometry of wave current case with varying force ($ALPHA = 2, t = 4T_w$)

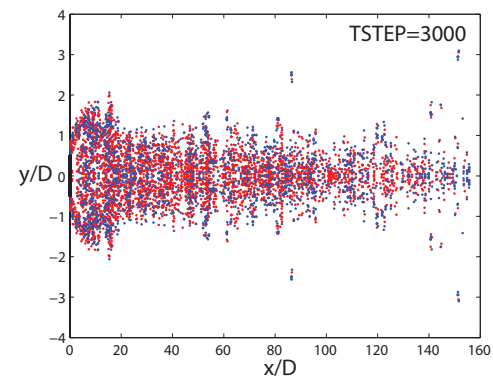


Figure 6-20: Wake geometry of wave current case with varying force ($ALPHA = 2, TSTEP = 3000$)

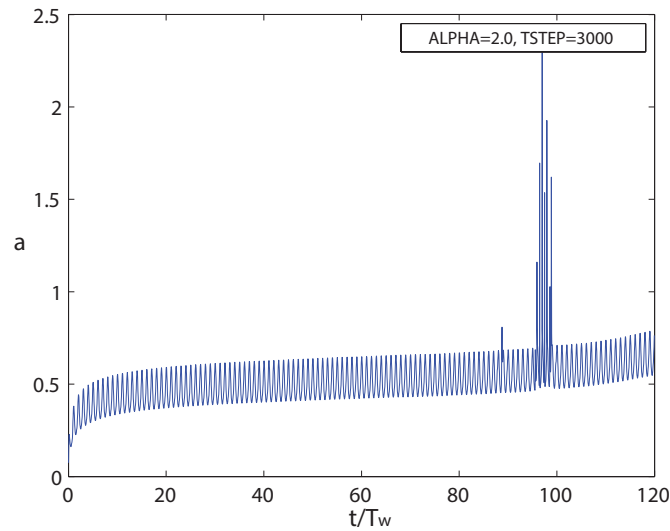


Figure 6-21: Induction factor of the wave and current case with varying force, $ALPHA = 2$

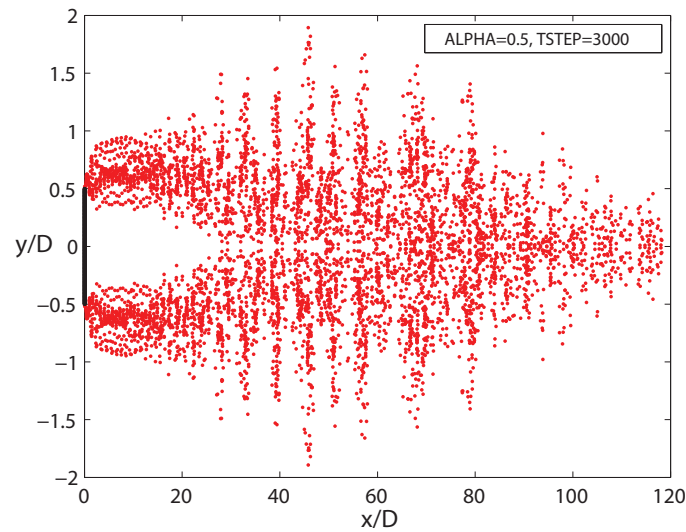


Figure 6-22: Wake geometry of the wave current case with varying force, $ALPHA = 0.5$

The induction factor here behaves similar to the case with constant force. It finally reach a periodic shape with a phase delay in comparison to U at the disk. The specific features of a from each case are discussed in the following part of the comparison with BEM.

Comparison with BEM

Similar to the analysis of induction factor in the case with constant force, the features of a and the relevant case parameters are shown in Table. 6-2. The shape of the periodic induction factor in this case is less similar to sinusoid, however, the period is still determined only by the wave period. The mean values of a are higher than the BEM theoretical value $a = 0.204$.

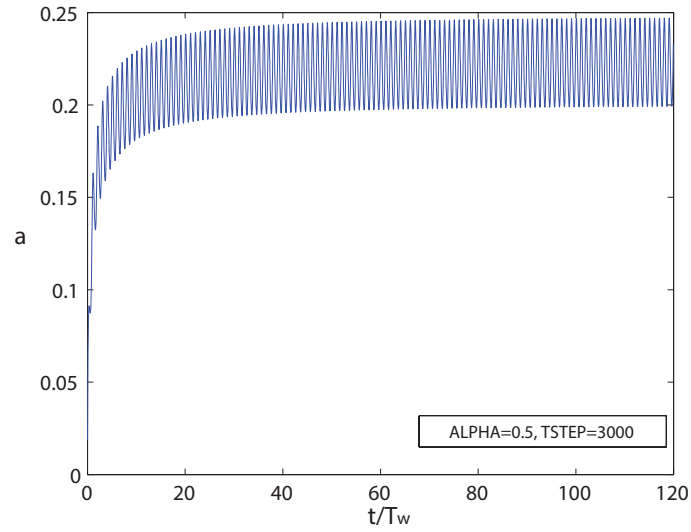


Figure 6-23: Induction factor of the wave current case with varying force, $ALPHA = 0.5$

Furthermore, it can be noticed that the larger the component ratio of wave, the higher the induction factor can reach. Why this happens remains unknown. In addition, for Case 2 and Case 3, the power output is always positive. Other cases with V_c slightly exceeds $AmpV$ are needed to check the possible negative power output. This can be done for the further study.

Case	T_w [s]	V_c [m/s]	ALPHA ($AmpV/V_c$)	a_{mean}	T_a [s]
2	5	1	0.2	0.2017	5
3	5	1	0.5	0.2230	5
4	5	1	1	0.3068	5

Table 6-2: Induction factor features of different wave current cases with varying force

Simulations for Different Wave Current Cases - 2D VAT

Results from the VAT model simulation are presented in this chapter. Since in the actuator disk model, the turbine is operating in a light-load situation, $C_T = 0.65$, the VAT is then chosen to contain two NACA0015 airfoils and operated with a tip speed ratio, $TSR = 5$. The chord of the blade is at the quarter chord and normal to the rotation radius. The chord to radius ratio is $c/R = 0.1$ with the rotation radius set as $R = 10m$ and the time step is $\Delta t = \frac{2.5^\circ}{\omega}$.

The geometry, angle of attack and the force data obtained from the simulation are presented for each case of different wave current scale. It is observed that after the 20th initial rotation, the blade load reaches a periodic manner. Thus, the results demonstrated here correspond to the situation after 20 rotations.

7-1 The current case

With merely the current, the VAT actually operates in a steady flow condition and the simulation returns the results similar to the one modeled with the original panel code [14]. The non-dimensional force coefficient on the x direction is defined as $C_{Fx} = \frac{F_x}{1/2\rho U_{ref}^2}$, with the reference velocity set as $U_{ref} = 1$. In one rotation (R), C_{Fx} and the angle of attack, α of the first blade behave in the manners shown in Fig 7-2 and 7-3.

7-2 Wave case

The simulation of the pure wave flow case is sub-divided into two parts. In the first part, the wave period is set to be $T_w = 5s$, same as the one of the actuator disk model. By doing so, we

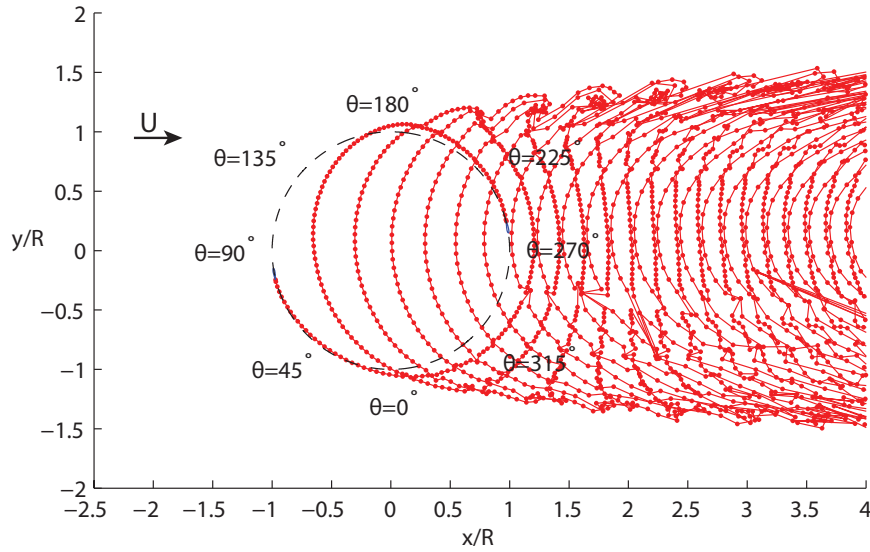


Figure 7-1: Wake Geometry of the VAT (Current Case)

try to simulate the situation where T_w has no clear relation with the turbine rotation period, T_R . While for the second part, we build the wave model with the assumption that the wave period is equal to the rotation period, $T_w = T_R$. The results from the different simulation situations are then discussed separately.

7-2-1 Arbitrary wave period

The wake development process is demonstrated in Fig. 7-4 to Fig. 7-7. It can be seen from the figures, the vortices generated in this case accumulate within the region of the VAT rotation plane. This can be understood that since the income flow velocity is oscillating, there is

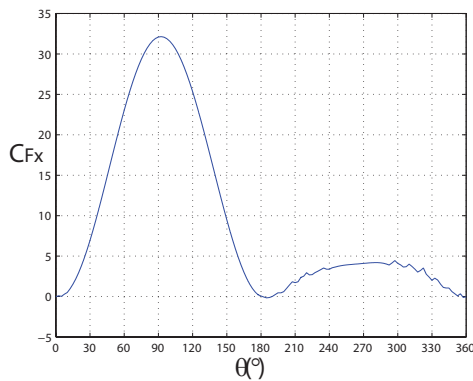


Figure 7-2: C_{F_x} over one rotation (Current Case)

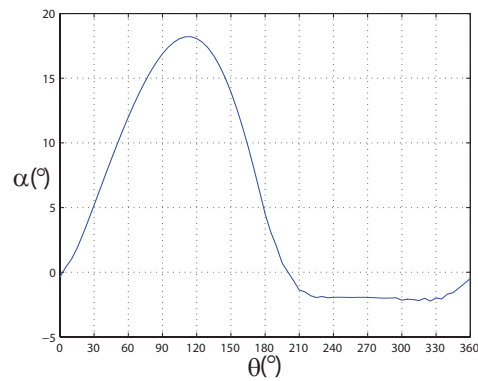


Figure 7-3: Angle of attack over one rotation (Current Case)

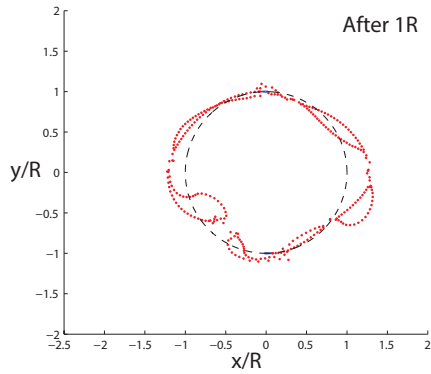


Figure 7-4: Wake geometry after 1 rotation (Wave Case, $T_w = 5s$)

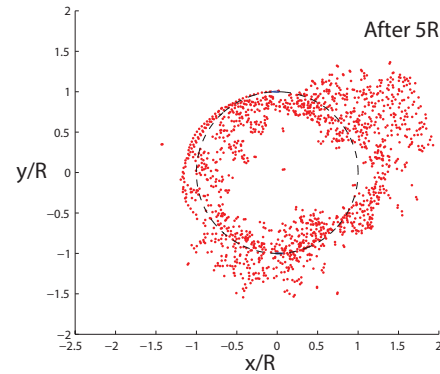


Figure 7-5: Wake geometry after 5 rotation (Wave Case, $T_w = 5s$)

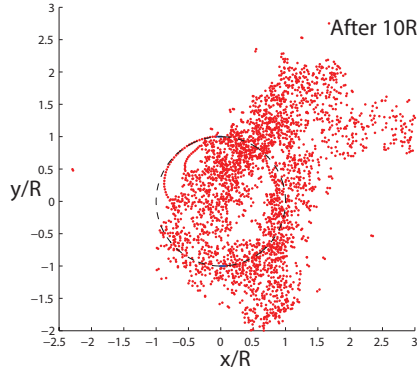


Figure 7-6: Wake geometry after 10 rotation (Wave Case, $T_w = 5s$)

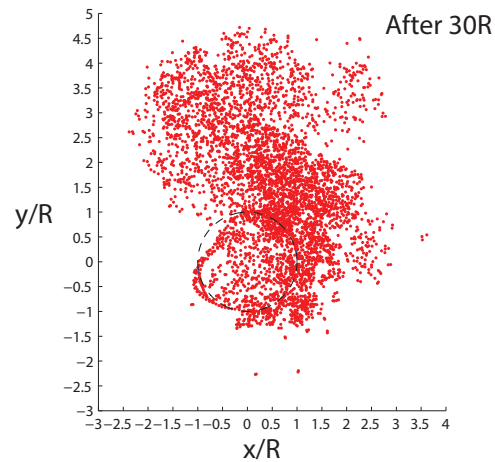


Figure 7-7: Wake geometry after 30 rotation (Wave Case, $T_w = 5s$)

no dominant velocity that can blow away the vortices. Their behaviors are quite chaotic and the x -component force coefficient also behaves randomly (see Fig. 7-8).

No useful power can be extracted from this case, some control strategies are needed to adjust the turbine operation. Since the blade of VAT is rotating, if we match the rotation period equal to the wave period, the velocity experienced by the blade at a specified azimuthal position will remain the same in each rotation. Under this circumstance, the turbine gives results with some regular rules, which are demonstrated in the next part.

7-2-2 Wave period equal to rotation period

The rotation period, T_R , can be computed from the definition of the tip speed ratio, $TSR = \frac{\Omega R}{U}$. With $TSR = 5$ in the coding, the rotation period of this turbine is 4π , around 12 s. Since this value is also within the wave period range of the sea area of the UK [17], we set the

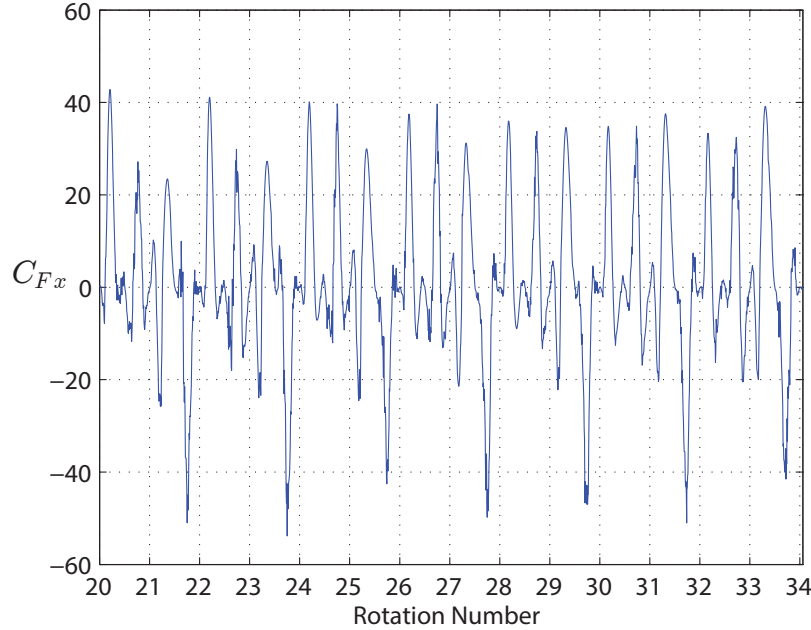


Figure 7-8: X-component Force Coefficient (Wave Case, $T_w = 5s$)

wave period equal to the rotation period, $T_w = T_R = 4\pi$. Then, we vary the starting phase of the wave model to control the income velocity perceived by the blade during the rotation. Four typical starting phase are chosen here, 0 , $\frac{1}{2}\pi$, π and $\frac{3}{2}\pi$. Fig. 7-9 to Fig. 7-12 illustrate the wake geometries obtained with the different starting phases.

There are still no clear wake structures in the geometries of these cases. However, the vortices travel downstream instead of staying in the rotor area. It is yet not clear that why without a dominant velocity on positive x direction, most of the vortices travel in a dominant direction. Further study that traces the vortex traveling is recommended to explain the formation of the wake and the results here mainly focus on the load behavior. The x component force coefficient, C_{Fx} , has a periodic shape with some sectional variations for all the starting phases (Fig. 7-13 to Fig. 7-16).

From the figures, we can see that C_{Fx} in the case with zero starting phase is negative for the most part of the rotation. Whereas, the π starting phase case returns an almost opposite results while the other two cases are in between. Therefore, we first trace the C_{Fx} (Fig. 7-17) and α (Fig. 7-18) of one rotation for the case with the starting phase equal to 0 to understand the cause of the negative C_{Fx} . Blade local geometries and the velocities perceived by the blade at four azimuthal positions are presented to study the relationship between the velocities. The four azimuthal positions are $\theta = 45^\circ$, $\theta = 135^\circ$, $\theta = 225^\circ$ and $\theta = 315^\circ$.

In Fig. 7-19 to Fig. 7-22, the black vectors represent the relative velocities, V_{rel} , while the blue ones are the velocities due to the displacement of the blade, V_{dis} . The flow velocities, V_{flow} at the quarter chord point are in red and the wake induced velocities, V_{wake} are shown

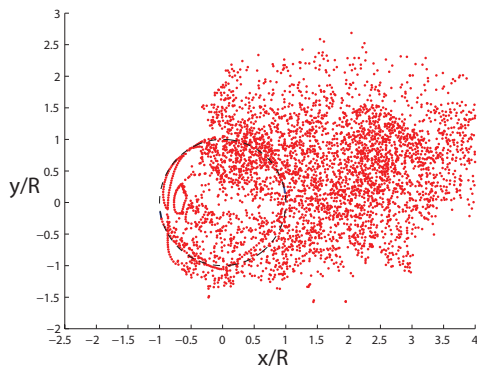


Figure 7-9: Wake geometry of the wave case with $T_w = T_R$ (Start 0)

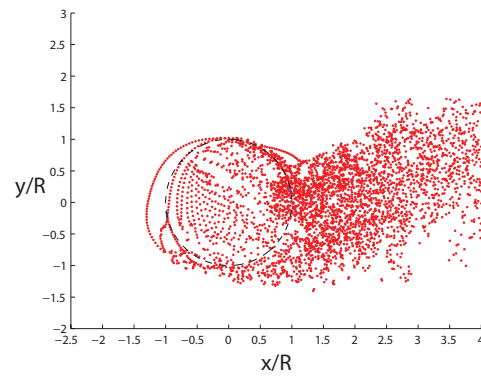


Figure 7-10: Wake geometry of the wave case with $T_w = T_R$ (Start $\frac{1}{2}\pi$)

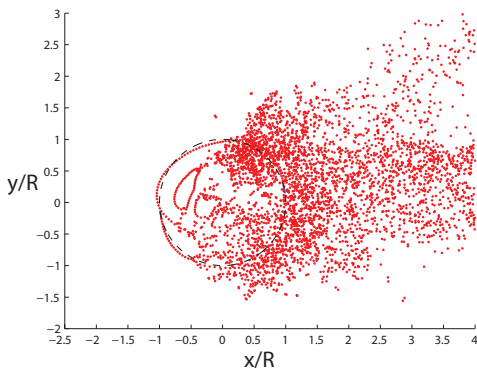


Figure 7-11: Wake geometry of the wave case with $T_w = T_R$ (Start π)

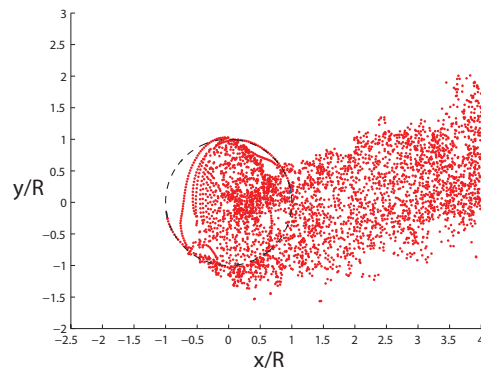


Figure 7-12: Wake geometry of the wave case with $T_w = T_R$ (Start $\frac{3}{2}\pi$)

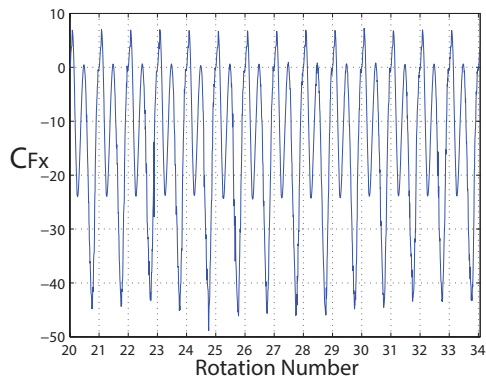


Figure 7-13: C_{Fx} of the wave case with $T_w = T_R$ (Start 0)

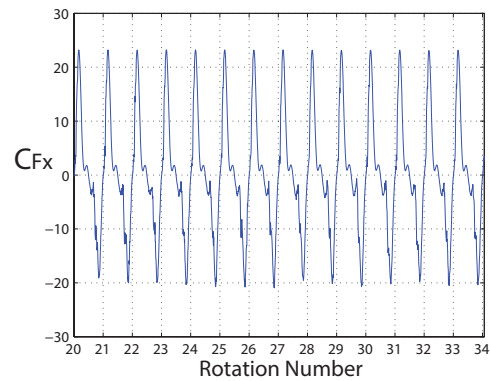


Figure 7-14: C_{Fx} of the wave case with $T_w = T_R$ (Start $\frac{1}{2}\pi$)

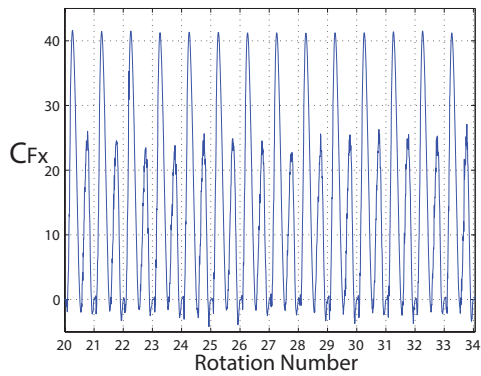


Figure 7-15: C_{Fx} of the wave case with $T_w = T_R$ (Start π)

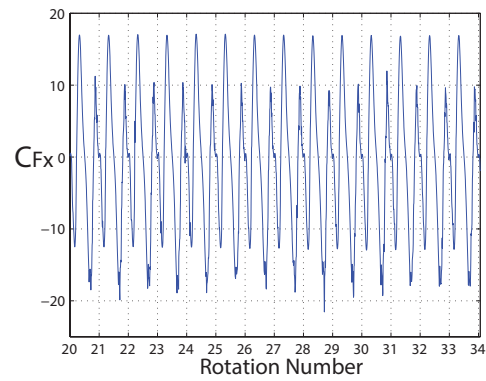


Figure 7-16: C_{Fx} of the wave case with $T_w = T_R$ (Start $\frac{3}{2}\pi$)

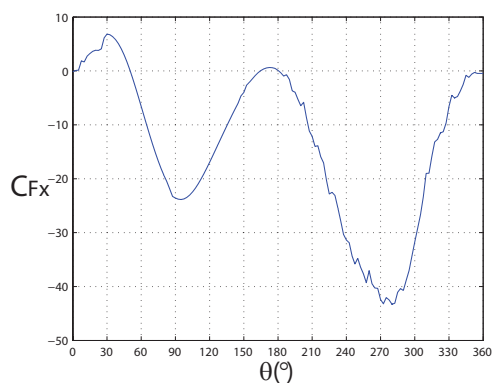


Figure 7-17: C_{Fx} over one rotation of the wave case, $T_w = T_R$ (Start 0)

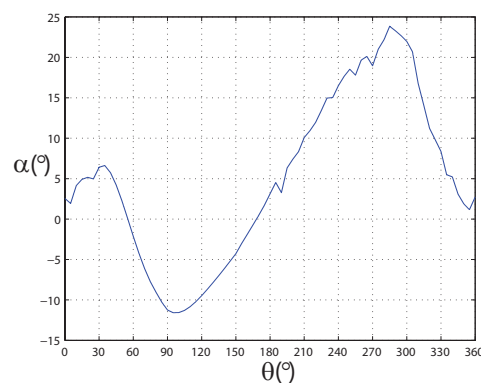


Figure 7-18: α over one rotation of the wave case, $T_w = T_R$ (Start 0)

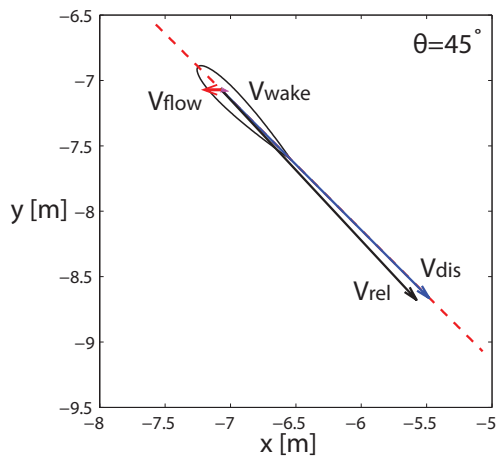


Figure 7-19: Velocities relation of the wave case with $T_w = T_R$ (Start 0, $\theta = 45^\circ$)

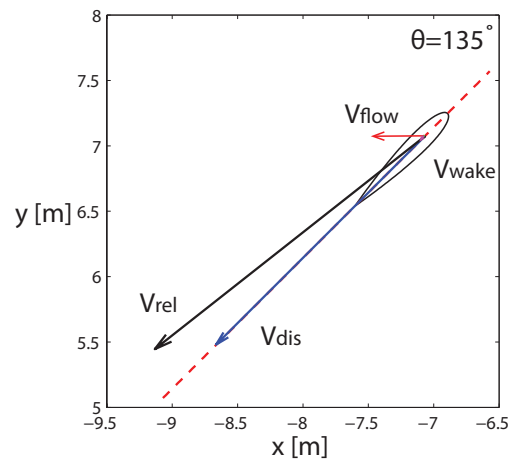


Figure 7-20: Velocities relation of the wave case with $T_w = T_R$ (Start 0, $\theta = 135^\circ$)

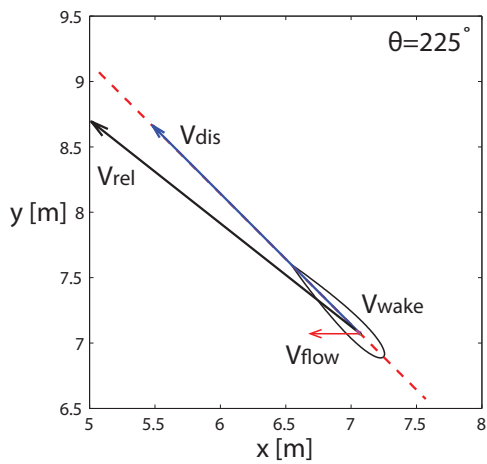


Figure 7-21: Velocities relation of the wave case with $T_w = T_R$ (Start 0, $\theta = 225^\circ$)

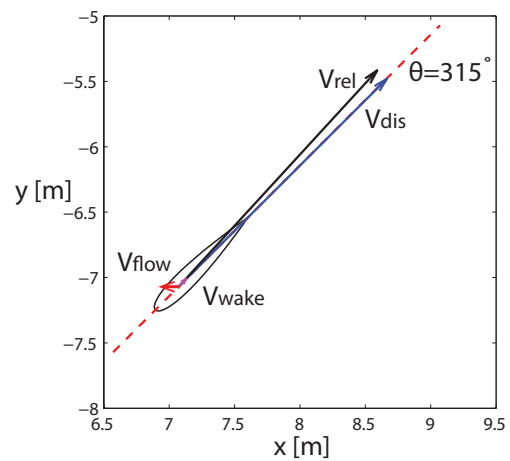


Figure 7-22: Velocities relation of the wave case with $T_w = T_R$ (Start 0, $\theta = 315^\circ$)

in purple. The velocities induced by the other airfoil are plotted green. However, they are negligible in comparison to other velocities and thus are not obviously detected in the figures. The red dash lines are the chord lines.

As illustrated from the figures, V_{dis} is always pointing the chord line direction. The main vector that influences the deviation of V_{rel} from the chord line is the flow velocity. In the 0 starting phase case, for all the four azimuthal positions, the V_{flow} points to the negative x direction, which results in the negative angle of attack in the upwind part ($0^\circ < \theta < 180^\circ$) and positive α in the downwind part ($180^\circ < \theta < 360^\circ$). This explains why the x -component force is almost negative in Fig. 7-13.

Then, to further explain the different blade loads in the cases with different starting phases. The azimuthal position with $\theta = 45^\circ$ is chosen to observe the velocity relationships from the four cases (Fig. 7-23 to Fig. 7-26).

Comparing these four cases in pairs, start 0 with start π and start $\frac{1}{2}\pi$ with start $\frac{3}{2}\pi$, according to the features of the sinusoid curve, the difference of π in the starting phase results in the opposite velocities in the cases of one pair. Since the flow velocity is the main influence factor of α , the angles in one pair are almost opposite to each other. However, the effect from the wake induced velocity is not negligible, especially when the wave velocity is in the zero-crossing area. This can further explain why C_{Fx} in one pair (for example, Fig. 7-14 and Fig. 7-16) are not just reversed. In addition, we may guess that V_{wake} is also the main cause of the sectional variation in the blade load.

The results in this case implicate that VAT can be utilized to extract energy from the pure wave oscillation. However, the strict control strategy is required to match the rotation period with the wave period. Moreover, the phase difference between the wave and blade rotation influences the load output. The negative x -component force may appear, which can be eliminated by pitching the blade during the rotation.

7-3 Wave and current case

Same as the previous section, the results are discussed separately according to the wave period.

7-3-1 Arbitrary wave period

When the wave velocity takes the dominant place, $ALPHA \geq 1$, the geometry and blade load behave similar as the case with pure wave oscillating. No regular rules can be found from the results and thus will not be further explained here

In the cases where $ALPHA < 1$, periodic responses with some randomness can be observed from the VAT model. The typical wake geometry and the x -component force coefficient

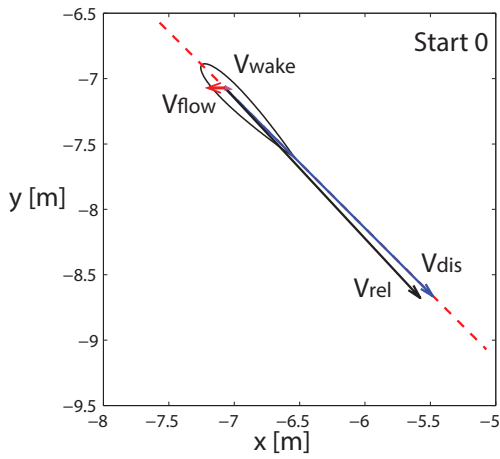


Figure 7-23: Velocities relation of the wave case with $T_w = T_R$ ($\theta = 45^\circ$, Start 0)

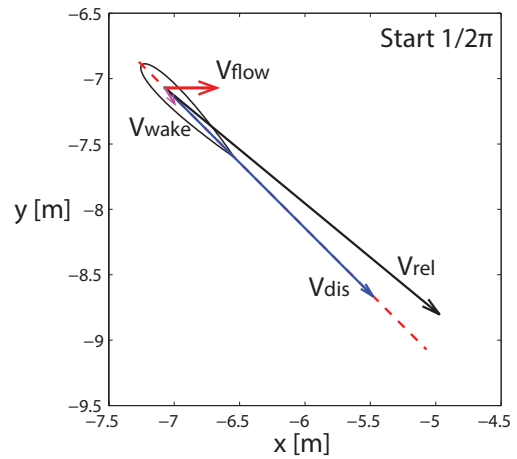


Figure 7-24: Velocities relation of the wave case with $T_w = T_R$ ($\theta = 45^\circ$, Start $\frac{1}{2}\pi$)

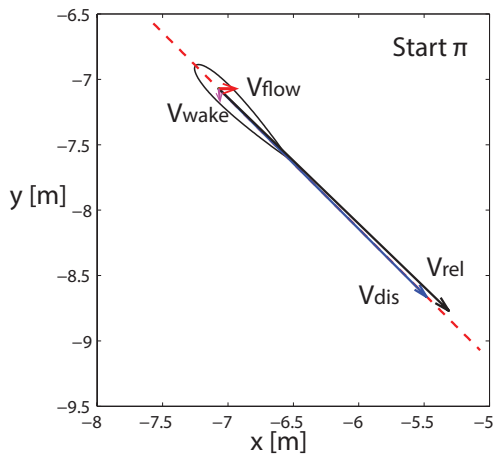


Figure 7-25: Velocities relation of the wave case with $T_w = T_R$ ($\theta = 45^\circ$, Start π)

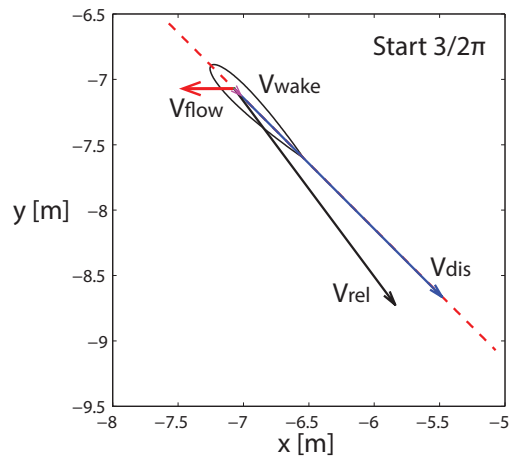


Figure 7-26: Velocities relation of the wave case with $T_w = T_R$ ($\theta = 45^\circ$, Start $\frac{3}{2}\pi$)

are shown in Fig. 7-27 and 7-28 for the case when $ALPHA = \frac{AmpV}{V_c} = 0.2$. The C_{Fx} curve illustrates that the downwind part is more sensitive to the velocity variation. This is explainable since the blade traveling downwind is operating in the wake of the upwind part while the vortex traveling speed is also influenced by the flow velocity as explained in Chapter 4.

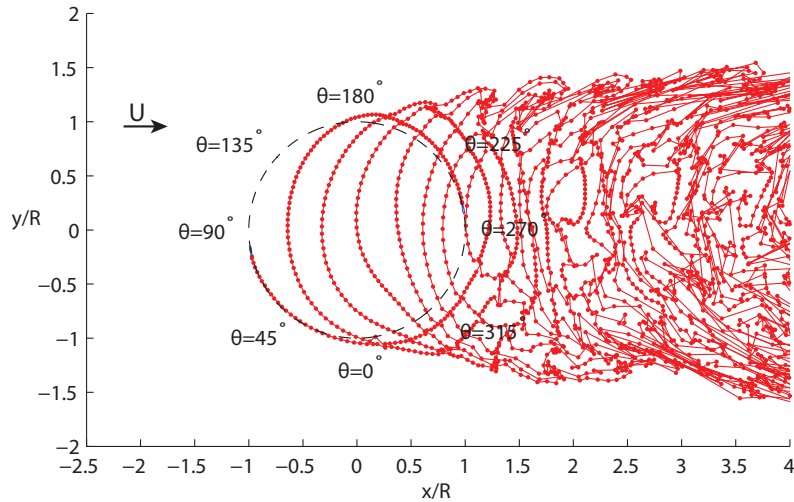


Figure 7-27: Wake Geometry of the wave current case with $T_w = 5s$ ($ALPHA = 0.2$)

7-3-2 Wave period equal to rotation period

With the integration of the current, the response from the turbine is improved in comparison to the results with pure wave oscillation. Since the negative part of the total income velocity become smaller due to the integration of the current flow, the occurrence of the negative angle of attack is also less. When $ALPHA \geq 1$, the negative velocity disappears. Regular wake structures which are similar to the one of the steady current flow case can be observed. The wake geometries and C_{Fx} curves from all the cases are similar. Thus, we only present the one in which $ALPHA = 0.2$ with starting phase equals π here.

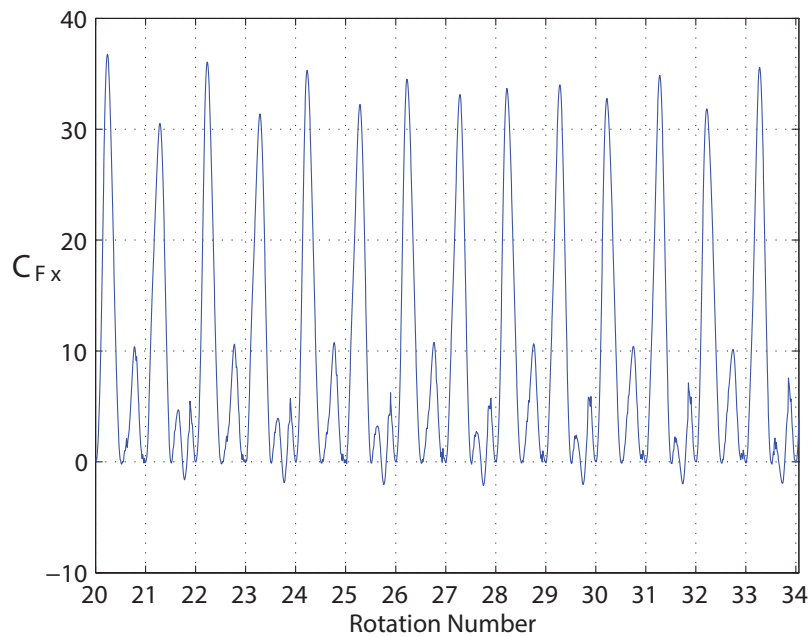


Figure 7-28: C_{Fx} of the wave current case with $T_w = 5s$ ($ALPHA = 0.2$)

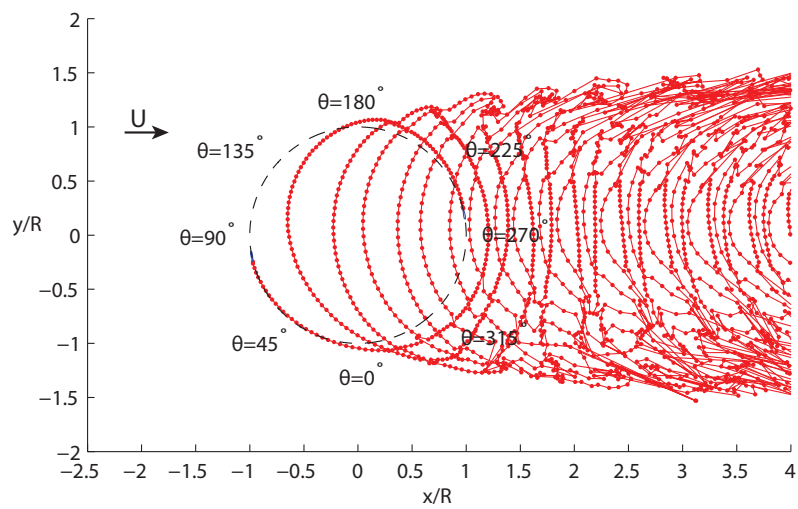


Figure 7-29: Wake Geometry of the wave current case with $T_w = T_R$ ($ALPHA = 0.2$, Start π)

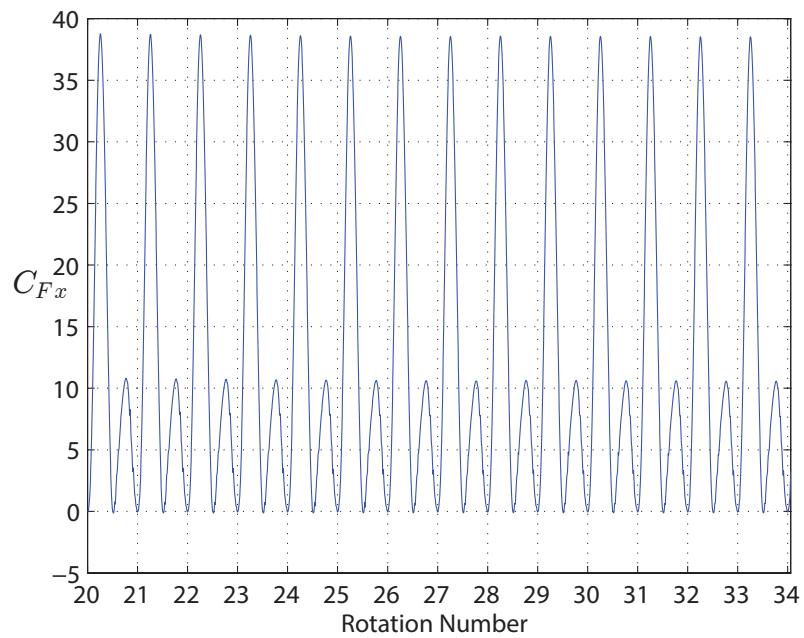


Figure 7-30: C_{Fx} of the wave current case with $T_w = T_R$ ($ALPHA = 0.2$, Start π)

Conclusions and Recommendations

This project consists of two models, the 2D actuator disk and the VAT rotor model. Results of case studies from those two models are discussed in the previous chapters. Now, we try to make a summary based on the observations. Section 8-1 will focus on the conclusions from the results of the case studies while Section 8-2 will discuss about the improvements and interesting findings that can be studied in the future work.

8-1 Conclusions

Firstly, results from the actuator disk model indicate that it is more feasible to install the cross flow actuator in the wave current flow where the current is dominant. For the pure wave flow, no regular power output is found and the turbine may be operated under the risk of large turbulence due to the vortices traveling back to the rotor area. When the current is added to the flow while the wave remains dominant, periodic power output can be obtained under the operation condition with constant force. However, some parts of the generated power are negative due to the negative resultant velocity perceived by the disk. In the cases with varying force applied on the disk, the vortices may also travel back to the rotor and bring large unsteady variations to the flow. Then, only for the situations where the current takes dominant place, the turbine will give responses which indicate the possibility of energy extraction. In addition, for all the unsteady cases, BEM fails to predict the unsteady response.

The VAT model shows the potential to collect energy from all the wave current combinations. However, strict control strategy is required to match the blade rotation period equal to the wave period. Based on the study of the load behaviors for the cases where the wave is simulated with different starting phases, the conclusion can be made that it is possible to control the load output by tuning the phase difference between the wave and the blade rotation. Furthermore, the blade pitch control can be applied to prevent any negative x component

force.

As summarized above, for all the cases where the energy extraction is possible, the turbine's performance will finally reach a regular periodic manner. However, the periodic response also means the possible fatigue damages, especially in the marine field with the high fluid density. Thus, how to overcome the serious fatigue problem will be a key challenge for the application of the marine turbine in the wave current unsteady flow.

8-2 Recommendations

This section first proposes the improvements that can be applied for the optimization of the numerical model. Then, the findings and ideas during the research period are demonstrated which may be interesting for the further study.

1. All the cases simulated in both models only consider the light-load condition. It is thus recommended to first validate the actuator disk model for the heavy load region and then simulate the situation under this load condition. The VAT model with three blades can then also be simulated.
2. For the actuator disk model, a cut-off vortex kernel and the Runge-Kutta method are applied to refine the code. However, from the comparison with BEM, especially in the high-load region, the deviation is not negligible. To improve the accuracy of the model, other kernel methods can be integrated, for example, the Lamb-Oseen. Furthermore, the higher order numerical methods and the time derivative method can help to further optimize the coding.
3. The actuator disk model is time consuming and requires several hours (in our case, 2 hours) to reach a regular periodic result. Fast multiple method (FMM) and Graphic Processing Unit (GPU) computation can be introduced to accelerate the computation process.
4. The BEM model proposed here for comparison is the classical BEM which can not predict the unsteady performance. Other unsteady models, for example, the dynamic inflow model can be applied for a better comparison.
5. During the study of the induction factor from the actuator disk model, it is found that when the induction factor behavior reaches the periodic manner, its variation follows some rules. Since the number of the case studies is limited, it is not sufficient to understand the exact influence on the oscillation of the induction factor. Further cases can be studied which may lead to interesting results.

6. In the VAT model, there are cases in which we assume that the wave period is equal to the rotation period, which requires strict control strategy in practice. Furthermore, since the turbine's response is periodic, how to apply the control method to efficiently extract energy remains a challenge for the future study.

Bibliography

- [1] J. Manwell, J. McGowan, and A. Rogers, *Wind Energy Explained*. John Wiley and Sons, Ltd, Publication, 2009.
- [2] D.V.Reddy and M. Arockiasamy, *Offshore Structures*. Krieger Publishing Company, 1991.
- [3] J. van Der Tempel, *Design of support structures for offshore wind turbines*. PhD thesis, Technische Universiteit Delft, 2006.
- [4] G. van Kuik, "The edge singularity of an actuator disc with a constant normal load," in *The 22nd AIAA/ASME Wind Energy Symposium*, 2003.
- [5] G. B. D. of Trade, Industry, G. B. E. T. S. Unit, R. G. U. C. for Environmental Engineering, and S. Energy, "A scoping study for an environmental impact field programme in tidal current energy," tech. rep., The Robert Gordon University, 2002.
- [6] B. Drew, A. R. Plummer, and M. N. Sahinkaya, "A review of wave energy converter technology," *Power and Energy*, vol. 223, pp. 887–902, 2009.
- [7] A. Bahaj and L. Myers, "Fundamentals applicable to the utilisation of marine current turbines for energy production," *Renewable Energy*, vol. 28, no. 14, pp. 2205 – 2211, 2003.
- [8] L.S.Blunden and A.S.Bahaj, "Tidal energy resource assessment for tidal stream generators," *Power and energy*, vol. 221, pp. 137–146, 2006.
- [9] P. D. Komar, *Beach Processes and Sedimentation-Second Edition*. Prentice Hall, 1997.
- [10] S. H. Salter, "Wave power," *Nature*, 1974.
- [11] Parliament, "Wave and tidal energy," tech. rep., Parliament, May 2001.
- [12] W. Batten, A.S.Bahaj, A. Molland, and J.R.Chaplin, "Hydrodynamics of marine current turbines," *Renewable energy*, vol. 31, pp. 249–256, 2006.

- [13] A. Bahaj, A. Molland, J. Chaplin, and W. Batten, “Power and thrust measurements of marine current turbines under various hydrodynamic flow conditions in a cavitation tunnel and a towing tank,” *Renewable Energy*, vol. 32, no. 3, pp. 407 – 426, 2007.
- [14] C. Simão Ferreira, *The near wake of the VAWT*. PhD thesis, Technische Universiteit Delft, 2009.
- [15] B. . V. Limited, “Tidal stream energy resource and technology summary report,” tech. rep., Carbon Trust, 650 London Road and Isleworth, Middlesex TW7 4EG and United Kingdom, July 2005.
- [16] <http://www.renewables-atlas.info/>, 2013. [Online; Date of access (26 August 2013)].
- [17] ABPmer, “Atlas of uk marine renewable energy resources,” tech. rep., ABPmer, March 2008.
- [18] C.Beels, J. Henriques, J. Rouck, M.T.Pontes, G. Backer, and H. Verhaeghe, “Wave energy resource in the north sea,” in *Proceedings of the 7th European Wave and Tidal Energy Conference*, 2007.
- [19] G. van Kuik, “Steady and unsteady actuator disc flows,” in *Proceedings of the seventh IEA symposium on the aerodynamics of wind turbine*, 1993.
- [20] K. Atkinson, *An Introduction to Numerical Analysis, 2nd Edition*. John Wiley & Sons, 1989.
- [21] J. Katz and A. Plotkin, *Low-speed Aerodynamics*. McGraw-Hill, 1991.
- [22] P.J.Moriarty and A.C.Hansen, “Aerodyn theory manual,” tech. rep., NREL, 2005.

Nomenclature

V_c	current flow velocity [m/s]
P_c	power contained in the current flow [W]
ρ	fluid density [kg/m^3]
A	turbine cross sectional area [m^2]
H	instantaneous wave height [m]
T_w	wave period [s]
H_s	significant wave height [m]
T_s	significant wave period [s]
P_w	power contained in the wave flow [W]
g	gravitational acceleration [m/s^2]
W	wave front width [m]
C_T	thrust coefficient
T	thrust [N]
P	kinetic power [W]
\dot{m}	mass flow rate [kg/s]
U	income flow velocity [m/s]
a	induction factor
C_P	power coefficient
Ω	rotor angular velocity [rad/s]
ω_{wake}	wake rotation velocity [rad/s]
a'	angular induction factor
r	local radius [m]
Q	torque [Nm]
ϕ	angle of the relative flow velocity [rad]
β	local pith angle [rad]
ϕ	angle of attack [rad]
F_L	lift force [N]
F_D	drag force [N]
F_N	force normal to the rotation plane [N]
F_T	force tangential to the rotation plane [N]
U_{rel}	relative velocity [m/s]
c	chord [m]

R	rotor radius [m]
C_l	lift coefficient
C_d	drag coefficient
B	number of blades
\mathbf{v}	velocity vector [m/s]
p	static pressure [Pa]
\mathbf{f}	force density distribution [N]
ω	vorticity [$1/s$]
ϵ	cross section thickness of the disk [m]
Γ	circulation strength [m^2/s]
\mathbf{V}	induced velocity [m/s]
\mathbf{V}_{res}	resultant speed [m/s]
$TSTEP$	number of the time steps
u	induced velocity on x direction [m/s]
v	induced velocity on y direction [m/s]
L	wavelength [m]
η	free surface elevation [m]
d	still water depth [m]
ω	circular frequency [rad/s]
k	wave number
C	wave propagation velocity [m/s]
$AmpV$	amplitude of the wave velocity on x direction [m/s]
V_{msp}	mean spring peak velocity [m/s]
σ	source strength [m^2/s]
μ	doublet strength [m^2/s]
Φ_∞	free-stream potential [m^2/s]
Φ	perturbation potential [m^2/s]
Φ^*	total potential [m^2/s]
Φ_i^*	inner potential
U_t	tangential velocity [m/s]
Δl	distance between the two adjacent control points [m]
C_F	force coefficient
U_{ref}	reference velocity [m/s]
u_{disk}	induced velocity at the disk center [m/s]
TSR	Tip Speed Ratio
θ	azimuthal position [rad]
V_{flow}	flow velocity perceived by the blade [m/s]
V_{wake}	wake induced velocity [m/s]
V_{dis}	velocity due to displacement [m/s]